International Journal of Heat and Mass Transfer 162 (2020) 120376

Contents lists available at ScienceDirect

International Journal of Heat and Mass Transfer

journal homepage: www.elsevier.com/locate/hmt

# Prediction of behavior of triangular solar air heater duct using V-down rib with multiple gaps and turbulence promoters as artificial roughness: A CFD analysis

Rohit Misra[a,*], Jagbir Singh[a], Sheetal Kumar Jain[b,c], Sachin Faujdar[a], Muskan Agrawal[a], Arin Mishra[d], Pradeep Kumar Goyal[e]

[a] Department of Mechanical Engineering, Engineering College, Ajmer, India
[b] Department of Mechanical Engineering, MNIT Jaipur, India
[c] School of RAC Skills, Bhartiya Skill Development University Jaipur, India
[d] Department of Mechanical Engineering, VIT Vellore, India
[e] Department of Civil Engineering, Delhi Technological University, Delhi, India

ARTICLE INFO

*Article history:*
Received 12 March 2020
Revised 4 August 2020
Accepted 20 August 2020

*Keywords:*
Triangular duct
Nusselt number enhancement ratio
Eddy viscosity
Heat transfer enhancement
Helicity

ABSTRACT

In the current study, duct of equilateral triangular cross section having V-down ribs with multiple gaps and turbulence promoters as artificial roughness is analyzed and thermo-hydraulic response of duct is measured. For in depth analysis computational fluid dynamics analysis has been carried out using ANSYS FLUENT 19.0. Under the parametric variation part, effect of change in roughness parameters, viz., relative roughness pitch and angle of attack on thermohydraulic performance has been explored. Flow Reynolds number (Re) is systematically varied from 4,000 to 20,000. Proposed roughness proves its worth as its attachment over the absorber leads to an enhancement in Nusselt number and friction factor both, because of enhanced level of interaction among the fluid particles. Study reveals that upon varying the relative roughness pitch (P/e) from 8 to 14 and angle of attack from $45^0$ to $60^0$, maximum heat transfer rate is attained at P/e = 10 and $\alpha = 45^0$, respectively, irrespective of Reynolds number. Performance of the SAH with proposed roughness is found to be better than other type of roughness elements studied in recent past.



## 1. Introduction

Solar energy has been nurturing the lives of millions of species on the planet for millions of years. Unlike fossil fuels, solar energy is more abundantly available. The planet receives 10,000 times more energy in the form of sunlight than the annual consumption of entire humanity in all possible forms. The solar energy that is being received on the Earth's surface in enormous quantity can be converted into a form which is useful to us.

Solar energy, being a renewable source of energy is totally cost free, highly sustainable, inexhaustible and is available throughout the year. Using solar radiation as energy source can reduce the energy and cost bills up to a great extent. Replacing non-renewable energy sources with solar energy can also reduce the emission of $CO_2$ significantly. Utilization of solar energy in heaters and other applications such as cooking, drying, pumping, etc. lowers the electricity consumption. Wide application field of solar energy is attracting researchers and investors to access solar energy system which is clean and safe for heating purposes.

SAHs are used to heat up the air by trapping and absorbing the solar radiation using a glass glazing and an absorber plate. It's an established fact that the heat transfer from solar air heater having a smooth absorber plate is poor due to the formation of laminar sub-layer over the heated surface which inhibits the heat transfer. Researchers have also experimented with various cross section of the solar air heater duct such as triangular ducts, rectangular ducts, square ducts, and triangular ducts with rounded corners.

To enhance the heat transfer between the absorber plate and air two approaches can be used, one is to increase the surface area for heat transfer and other is to increase the convective heat transfer coefficient. Using artificial roughness on absorber plate increases the convective heat transfer by disrupting the laminar sub-layer

*Abbreviations:* SAH, Solar air heater; CFD, Computational fluid dynamics; NNER, Nusselt number enhancement ratio; FFER, Friction factor enhancement ratio; THPP, Thermo-hydraulic performance parameter.

* Corresponding author.
*E-mail address:* rohiteca@ecajmer.ac.in (R. Misra).

https://doi.org/10.1016/j.ijheatmasstransfer.2020.120376
0017-9310/

**Nomenclature**

| | |
|---|---|
| $D_h$ | hydraulic diameter, mm |
| W | duct width, mm |
| H | height of duct, mm |
| e | rib height, mm |
| g | gap size, mm |
| h | heat transfer coefficient, W/m$^2$-K |
| k | thermal conductivity of air, W/m-K |
| L | length of test section, mm |
| P | pitch, mm |
| u | velocity of air, m/s |
| *Greek symbols* | |
| $\alpha$ | angle of attack, $^\circ$ |
| $\mu$ | dynamic viscosity, Pa*s |
| $\rho$ | density of air, kg/m$^3$ |
| k | turbulent kinetic energy, m$^2$/s$^2$ |
| $\varepsilon$ | turbulent kinetic energy dissipation rate, m$^2$/s$^3$ |
| *Non-dimensional numbers* | |
| $e/D_h$ | relative roughness height |
| P/e | relative roughness pitch |
| W/H | aspect ratio |
| f | friction factor |
| $f_s$ | friction factor for smooth duct |
| $f/f_s$ | friction factor enhancement ratio |
| Nu | Nusselt number |
| $Nu_s$ | Nusselt number for smooth duct |
| $Nu/Nu_s$ | Nusselt number enhancement ratio |
| Re | Reynolds number |
| Pr | Prandtl number |
| St | Stanton number |

and promoting the turbulent flow inside the duct. In addition to this, these roughness patters also result in high pressure losses due to friction which creates the need of higher pumping power. Various studies are going on to find the effect of various roughness patterns on heat transfer coefficient and thermal efficiency.

During the last couple of years, researchers have showcased the findings of their studies carried out on air heater duct having variety of roughness elements.

Kumar et al. [1] scrutinized the fluid flow and heat transfer aspects of a triangular duct SAH experimentally as well as numerically. The investigation was conducted on three various models, viz. simple triangular duct, duct with rounded corners on one side, and duct with rounded corners on one side having roughness also. It was summarized that the triangular duct SAH with rounded corners on one side having roughened absorber plate gave the best performance. In one more experimental study, Kumar et al. [2] analyzed the thermal performance of a ribbed absorber plate having arc-shaped roughness. The roughness parameters including number of gaps, relative gap width and relative gap position, were systematically varied. Thermal performance of SAH was optimized by response surface methodology, and by executing so, it was reported that at relative gap width value of 1, relative gap position value of 0.6 and number of gaps value of 3, the best possible THP value was 3.85. Jain et al. [3] conducted a numerical study and determined the thermal performance of SAH, whose absorber surface was having discrete V-shaped perforated baffles as artificial roughness. The effect of relative blockage height (e/H) on Nusselt number (Nu), friction factor (f), and thermohydraulic performance parameter (THPP) was analyzed. Nusselt number enhancement ratio and friction factor enhancement ratio were claimed to be 4.24 and 14.73, respectively. However, a THPP having a maximum value of 2.24 was reported at e/H = 0.4. Kumar et al. [4] carried out a CFD analysis and investigated the thermo-hydraulic performance of circular rib roughened triangular passage SAH. Relative roughness pitch (P/e and Reynolds number (Re) were systematically varied. THPP was reported to be maximum at Re of 15000, P/e, and e/D were 12 and 0.06, respectively.

Jain et al. [5], using a CFD model, investigated the effect of broken inclined ribs having rectangular cross-section on THPP of equilateral triangular passage duct. In their CFD investigation, the effect of relative gap width and relative gap position was explored by varying the Reynolds number from 4000 to 18000. The study revealed that at d/w = 0.5 and g/e = 1, Nusselt number for roughened duct increased by 2.16 times, as compared to the smooth duct. In one more study by Jain et al. [6], the effect of arc-shaped ribs with multiple gaps on heat transfer augmentation in SAH was investigated using an experimental setup. Number of gaps ($N_g$) and Reynolds number (Re) was systematically varied, keeping heat flux constant at 1000 W/m$^2$. It was reported that for roughened SAH, the heat transfer and pressure drop were 274% and 169% higher than that obtained for smooth SAH. Further, the THPP with maximum value of 2.75 was reported.

Kumar et al. [7] carried out a numerical analysis based on FVM and investigated the heat transfer and flow field characteristics of ribbed 3-D SAH. Relative roughness height (e/D) was systematically varied, keeping relative roughness pitch at a constant value. It was reported that the THPP was observed to be highest with the value 2.08 at Reynolds number of 17,100. Patel and Lanjewar [8] presented the findings from their experimental work carried out on SAH duct having novel V-rib roughness geometry. The investigation included a rigorous parametric variation, including various roughness and flow parameters. The study claimed that maximum enhancement in Nusselt number was observed at P/e = 10, whereas friction factor was found to be maximum at P/e = 8 as compared to the smooth duct. Singh et al. [9] conducted a comparative study of enhancement in performance of Solar Air Heater with two different arrangements of ribs viz. multiple broken transverse ribs and square wave shaped ribs for the experimental as well as Numerical investigation purpose. It was pointed out in the study that for square-wave shaped ribs, thermal performance got enhanced by 2.5 times, and with multiple broken ribs, the enhancement in thermal performance was claimed to be 3.24 times as compared to the smooth duct. The study also pointed out that the above two roughness geometries improved the pumping power penalty also of the order of 3.92 times and 3.85 times as compared to smooth duct, respectively. Singh and Singh [10] carried out a simulation study using ANSYS Fluent 15 and investigated the THPP of SAH duct having non-uniform cross-sectioned square wave profiled transverse rib as artificial roughness. In the investigation, P/e was varied from 4 to 30, Reynolds Number from 3000-15000, keeping e/D fixed at 0.043. Maximum enhancement in Nu and f for roughened duct was reported to be 2.14 times and 3.55 times higher than that obtained for smooth duct SAH, respectively, at P/e = 10, Re = 15000, the maximum value of THPP was reported to be 1.43 at P/e = 10; Re = 12000.

Qader et al. [11] presented a CFD based simulation to conclude THPP, the average Nusselt number (Nu), and friction factor(f) on an artificially roughened SAH having inclined fins by varying slant angle and pitch (P). From outcomes, it was reported that maximum THPP of 1.916 was achieved at a value of $45^0$ slant angle and pitch value of 20 mm at Reynolds number 20,000. Jain and Lanjewar [12] investigated the thermal performance of solar air heater duct with V-rib having symmetrical gaps and staggered rib geometry. Roughness parameters including relative gap width (g/e), relative staggered rib pitch (P'/P), relative staggered rib size (w/e), and angle of attack ($\alpha$) were kept fixed. Relative roughness pitch (P/e) and Reynolds number (Re) were systematically varied, and it was ob-

served that at relative roughness pitch = 12, THPP was maximum. It was also concluded that Nusselt number and friction factor augmentation was 2.3 times and 3.18 times to that of smooth SAH. Perwez and Kumar [13] carried out an experimental investigation to determine the thermal performance of a spherical dimpled absorber plate and a flat absorber plate for several mass flow rate of air at IIT Dhanbad, India. It was reported that spherical dimpled absorber plate has 1.51 to 1.64 times higher rate of heat transfer than flat absorber plate. For 0.009 kg/s mass flow rate of air, they noted a rise of 4.6°C in outlet temperature of spherical dimpled SAH than flat plate SAH. The instantaneous thermal efficiency of the spherical dimpled absorber plate was about 23.45% to 35.50% higher than the flat-plate SAH. Kumar [14] explored the outcomes of an experimental investigation on 1 and 3-sided concave dimpled roughened absorber plate. On systematically varying relative dimple pitch (p/e), relative dimple height ($e/D_h$), relative dimple depth (e/d), it was noted that the maximum improvement in Nusselt number was 2.6 to 3.55, 1.91 to 3.42, 3.09 to 3.94 times and that of friction factor was of the order of 1.62 to 2.79, 1.52 to 2.34 17 and 2.21 to 2.56 times respectively over those of 1-sided roughened absorber plate.

Saravanakumar et al. [15] studied the impact of SAH integrated with arc-shaped rib roughened barrier with fins and baffles by varying the flow parameters and temperature rise parameters. It was discovered that at higher mass flow rates, maximum effective efficiency was delivered. Promvonge and Skullong [16] experimentally explored the thermal characteristics of SAH duct, in which a perforated/punched rectangular wing (P-RW) was mounted on the absorber plate. The study pointed out that attachment of P-RWs on the absorber plate could considerably increase the Nusselt number as corresponding to the smooth absorber plate. The rise in Nu and f for roughened absorber plate was claimed to be 3.91 to 5.52 times and 10.37 to 36.35 times, respectively, higher than that obtained for smooth absorber plate. The thermo-hydraulic performance was also declared to be highest, having a value of 2.01 for roughened SAH. Ambade and Lanjewar [17] carried out an experimental interpretation on SAH having new symmetrical gap arc geometry and staggered elements as roughness elements. Roughness parameters were orderly varied, and the performance of absorber plate roughened with proposed roughness elements was compared with the performance of the absorber plate having broken arc rib with staggered elements and with smooth absorber plate. The investigation declared a maximum increase in friction factor and Nusselt number by 3.88 and 2.18 times, respectively, as contrasted to the smooth plate at relative rib pitch of 10. Baissi et al. [18] conducted an experimental investigation to enhance the SAH thermal performance using two longitudinally curved delta-shaped baffles as artificial roughness on the absorber plate. The investigation was carried out for perforated and non-perforated baffles. The results asserted a notable improvement in heat transfer and pressure drop. Nusselt number and friction factor were mentioned to be 6.94 and 45.83 times higher than that achieved for smooth duct. Kumar and Layek [19] presented the outcomes of Liquid crystal thermography technique accompanying CFD, carried out to investigate the heat transfer through the absorber surface of the SAH. It was claimed that Nusselt number enhancement ratio was highest and equivalent to 1.97 at P/e = 10. Debnath et al. [20] conducted a numerical study to examine the fluid flow and heat transfer characteristics of a SAH, whose absorber surface was roughened with pentagonal ribs. Flow and roughness parameters were systematically varied, and the study claimed enhancement in Nusselt number and friction factor by 70% and 67.2%, respectively, at e/D = 2.045, P/e = 8, and Re = 38,414.

On comparing various cross-sections (square, circular, rectangular and semi-circular) of solar air heater duct, it is found that the triangular cross-sectional duct provides minimum frictional resistance to the fluid, consequently, requires minimum pumping power for fluid flow [21]. Despite being the best, as far as the pumping power requirement is concerned, triangular cross-section duct could not attract much attention of the researchers to investigate its behavior using various artificial roughness.

On reviewing the literature, it is pertinent to mention that the researchers keep on exploring the ways to attain higher and higher thermohydraulic performance of SAH by proposing variety of roughness elements to create turbulence near the absorber surface, which in turn enhances the heat transfer. It is concluded that on changing the shape (circular, square, V-grooved, semicircular etc.) and pattern (transverse, inclined, V down etc.) of rib elements, significant change in the value of Nu and f is observed. A study by Patel and Lanjewar [8] presented their experimental work on V rib roughness geometry comprised of broken V ribs with staggered elements. This investigation claimed NNER and FFER values to be 2.26 and 3.40, respectively, having a maximum THPP value of 1.59. In the present numerical study, authors attempt to enhance heat transfer using turbulence promoters instead of staggered elements and using solar air heater duct of triangular cross-section ensures reduced pumping power requirement which consequently, enhances THPP value. Novelty of the present work is that for the first time the performance evaluation of triangular solar air heater duct having a unique combination of V-down ribs with multiple gaps and turbulence promoters as artificial roughness underneath the absorber plate is being explored based on numerical investigation employing ANSYS FLUENT- 19. It is expected that this novel combination will be beneficial in terms of providing higher heat transfer rates with minimum rise in pumping power. Heated surface of triangular duct, with the proposed roughness is likely to result into greater turbulence in flow near the heated surface and much higher induced secondary flows. An in-depth CFD analysis has been conducted using ANSYS FLUENT (19.0) and thermohydraulic performance of roughened duct with proposed roughness geometry has been investigated and compared with the performance of triangular duct having smooth absorber surface. Moreover, the results of the present study have also been compared with the most recent similar type of studies carried out on solar air heater ducts with different artificial roughness geometries in terms of thermohydraulic performance parameter.

## 2. Description of CFD model

A 3-D model of triangular cross-sectioned duct of a solar air heater has been modelled using SOLIDWORKS (18.0). While, heat transfer characteristics and fluid flow attributes have been explored via Ansys Fluent (19.0). Each side of the triangular duct is 52 mm long as presented in Fig. 1. The duct is having three segments namely, Entrance section, Test section and Exit section, with length of 300 mm, 500 mm, and 200 mm, respectively as depicted in Fig. 2. While selecting the length of entrance section and exit section of duct due consideration was given to ASHRAE standards 93-77 [22], and accordingly, entrance and exit lengths have been kept greater than $5\sqrt{(W^*H)}$ and $2.5\sqrt{(W^*H)}$, respectively. It ensures the flow develops completely before it approaches the test section, and it involves least possible losses at the outlet section.

The entire volume of the duct has been meshed using a 3-D hybrid (Tetrahedral and Hexahedral) mesh. Regions close to ribs have been meshed using unstructured mesh because it analyses the laminar sub-layer region more precisely. Fig. 3 portrays the schematic of triangular duct having V-down rib with multiple gaps, having a cross-section as shown, which is a combination of tapered and circular profiles. Turbulence promoters are in the form of small segments in V-up pattern and are having a semi-circular cross-section.

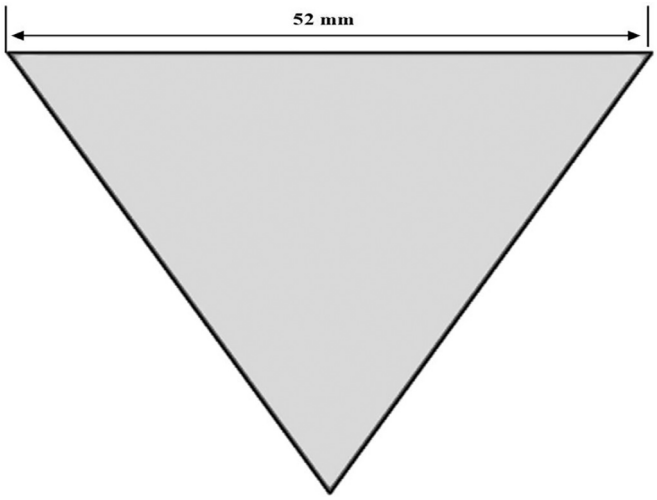


**Fig. 1.** Cross-section of equilateral triangular SAH duct.

Present CFD simulation work carries the following assumptions [23]: -

1) Incompressible and ideal fluid.
2) Negligible heat losses through the system.
3) No-slip condition at walls of the duct for velocity.
4) Temperature does not affect the thermo-physical properties like Prandtl number (*Pr*), viscosity, thermal conductivity, and density of fluid for the range of temperature that SAH is encountered with.

Table 1 illustrates the parameters considered in the current simulation study.

### 2.1. Grid independence test

The quality of computational zone which is modelled using a CFD tool can be analyzed by carrying out a grid independence test. Grid Independence test also guarantees that the model which has been developed is appropriate for further analysis. The solution is grid-independent, if upon refinement of the mesh, the solution does not change. In current CFD analysis, an unstructured mesh has been used, and mesh size has been refined from coarse to medium to fine mesh. Results of the analysis have been featured in terms of Nu and f at constant Re value of $10^{*}10^{3}$. A logical deduction was preferred for the results to be unbiased of the grid size by making the mesh finer and for that purpose, mesh elements were increased from 11,50,916 (coarse mesh) to 12,18,187 (medium mesh) to 14,35,053 (fine mesh), and the values of Nu and f were determined.

**Table 1**
Geometrical and roughness parameters used in simulation.

| S. No. | Parameters | Value(s) |
|---|---|---|
| 1 | Relative Roughness Pitch, P/e | 8, 10, 12, 14 |
| 2 | Angle of Attack, $\alpha$ | 45°, 50°, 55°, 60° |
| 3 | Hydraulic Diameter, $D_h$ | 0.03 m |
| 4 | Relative Roughness Height, $e/D_h$ | 0.04 |

As mentioned in Table 2, it is noted that a variation of less than 1% in the values of Nu obtained, when mesh size was increased from medium to fine. Therefore, to reduce the time required for the computation, medium size mesh was chosen for further parametric investigation.

### 2.2. Governing equations and justification of turbulence model

Provided below are the fundamental equations for the fluid flow, heat, and mass transfer:

Continuity equation:

$$\frac{\partial \rho}{\partial t} + \nabla \cdot (\rho u) = 0 \tag{1}$$

Momentum equation:

$$\rho \frac{\partial U_J}{\partial t} + \rho U_i \frac{\partial U_J}{\partial x_i} \nabla = -\frac{\partial P}{\partial x_j} - \frac{\partial \tau i_J}{\partial x_i} + \rho g \tag{2}$$

Energy equation:

$$\frac{\partial}{\partial x_j}\left[\rho u_j T\right] = \frac{\partial}{\partial x_j}\left[\left(\frac{\mu}{Pr} + \frac{\mu_t}{\sigma_t}\right)\frac{\partial T}{\partial x_j}\right] \tag{3}$$

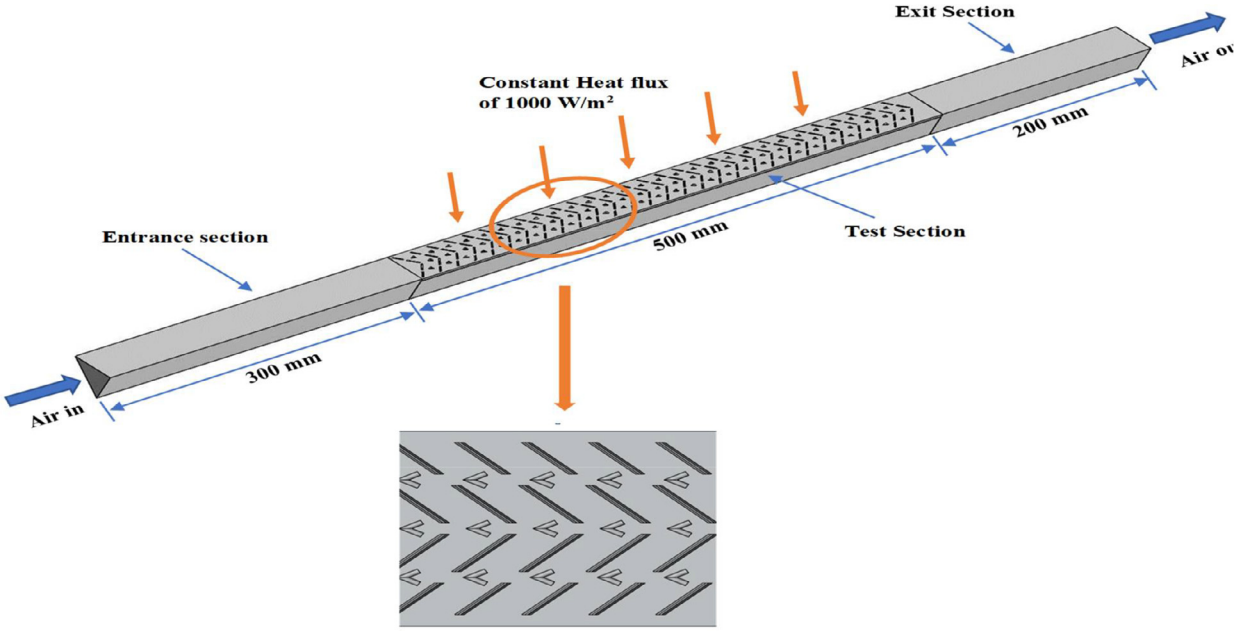


**Fig. 2.** Absorber plate with V-down rib with multiple gaps and turbulence promoters.

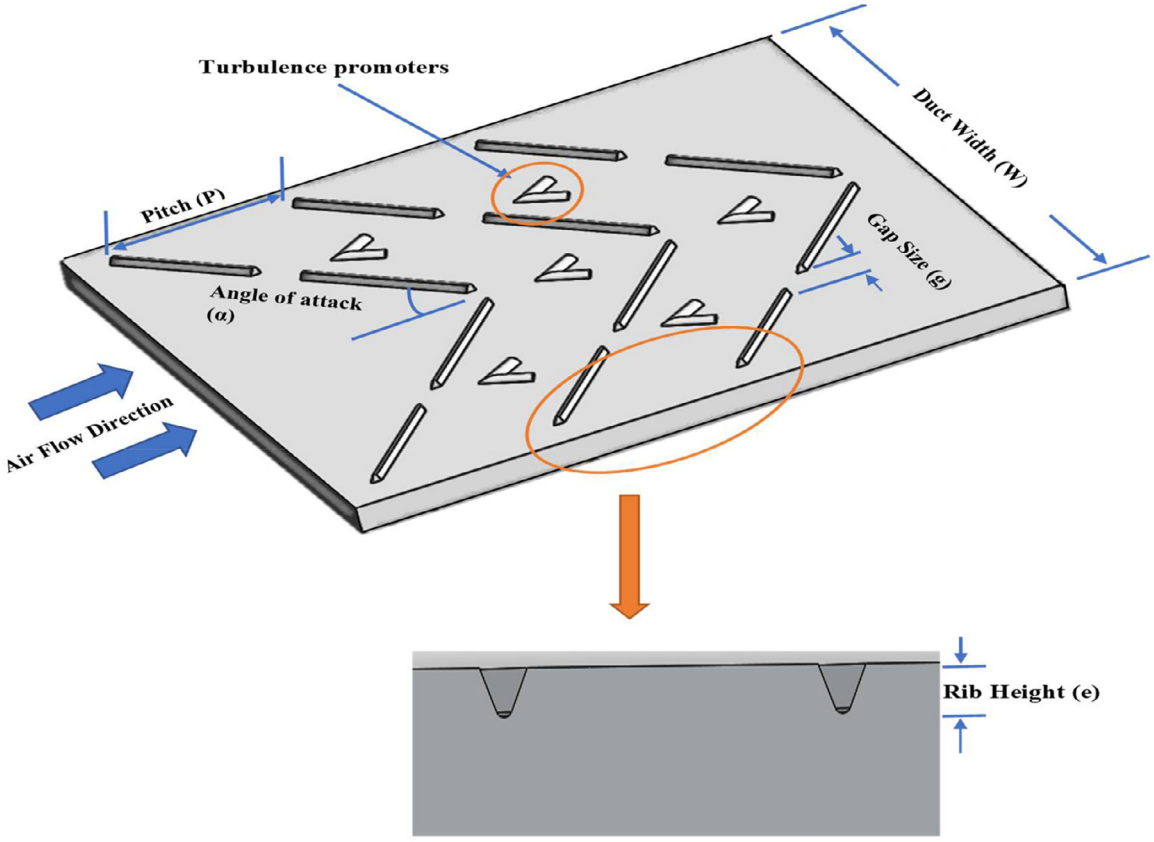


**Fig. 3.** Roughness pattern of V-down rib with multiple gaps and turbulence promoters.

**Table 2**
Percentage deviation in Nu and f with variation in number of grid elements.

| Number of grid elements | Re | Nu | f | Deviation in Nu (%) | Deviation in f (%) |
|---|---|---|---|---|---|
| 1150916 (Coarse Mesh) | 10000 | 36.2 | 0.0092 | - | - |
| 1190853 (Coarse Mesh) | 10000 | 35.4 | 0.0090 | 2.10 | 2.04 |
| 1218187 (Coarse Mesh) | 10000 | 34.9 | 0.0089 | 1.30 | 1.32 |
| 1315323(Medium Mesh) | 10000 | 34.5 | 0.0088 | 0.54 | 0.34 |
| 1435053 (Fine Mesh) | 10000 | 34.3 | 0.0088 | 0.29 | 0.18 |

Where i and j represents directional components.

### 2.3. Validation of simulation model

For carrying out CFD analysis, several turbulence models are incorporated in ANSYS Fluent (19.0) [24] viz. Standard k-$\varepsilon$ model, RNG k-$\varepsilon$ model, Realizable k-$\varepsilon$ model, Standard k-$\omega$ model, Reynolds Stress model, Spalart-Allmaras model and SST k- $\omega$ model. To explore the most appropriate and best suitable turbulence model for detailed CFD study, the values of Nu and f examined using these models for smooth SAH duct and theoretical values computed using Dittus-Boelter equation and Blasius equation, respectively, were compared. Dittus-Boelter equation and Blasius equation are given by Eqs. (4) and (5), respectively.

$$Nu_s = 0.024\ Re^{0.8}Pr^{0.4} \tag{4}$$

$$f_s = 0.085\ Re^{-0.25} \tag{5}$$

It is noticed from Figs. 4 and 5 that RNG k-$\varepsilon$ model comes out with an average deviation of 4.29% and 5.7% between simulated and theoretical values of Nu and f, respectively. Thus, based on least variation observed between simulated and theoretical values of Nu and f, RNG k-$\varepsilon$ turbulence model with standard wall function has further been used for detailed parametric analysis.

To validate the present CFD model, the results of CFD investigations have been compared with the experimental results presented by Rajneesh et al. [1] for smooth triangular SAH duct. Fig. 6 shows the contrast between Nu value and f value computed by CFD approach used in current analysis and results ascertained experimentally by Rajneesh et al. [1]. It is noticed from Fig. 6 that the Nu and f values estimated by present CFD model are having a good match with the experimental results. The maximum deviation of CFD based Nu and f from experimental results is in the range of ± 6% and ± 4%, respectively. The deviation of CFD based results from the experimental findings is in acceptable range and therefore, the present CFD approach can be employed for the further numerical investigation and parametric analysis.

### 2.4. Boundary conditions and solution approach

In the current simulation study, boundary conditions [25] that have been employed, are portrayed in Table 3.

Residuals for the X, Y and Z velocity; continuity; energy; turbulent kinetic energy (k); turbulent kinetic energy dissipation rate (ε)

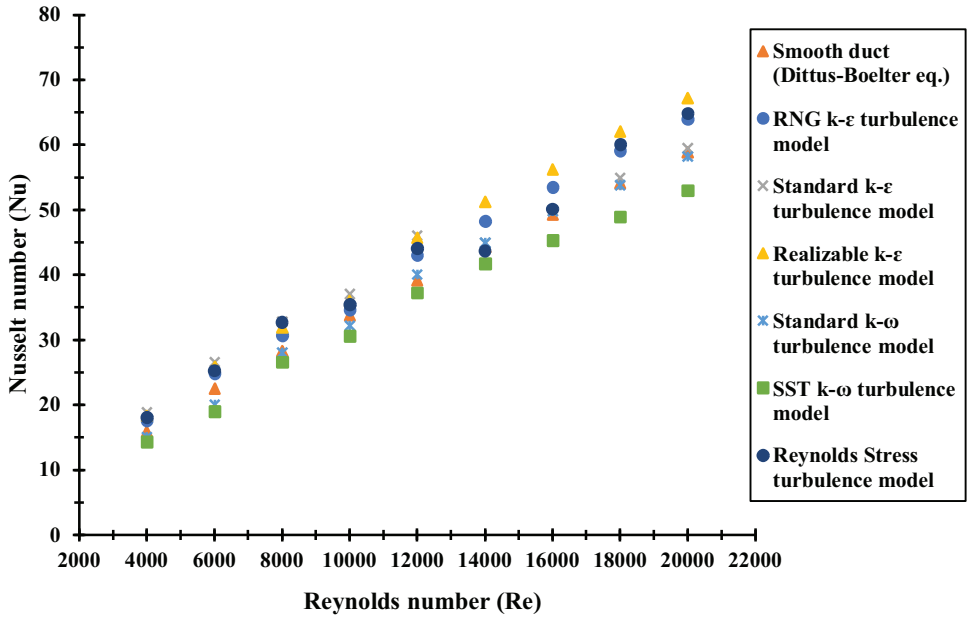


**Fig. 4.** Nusselt number validation for smooth SAH duct.

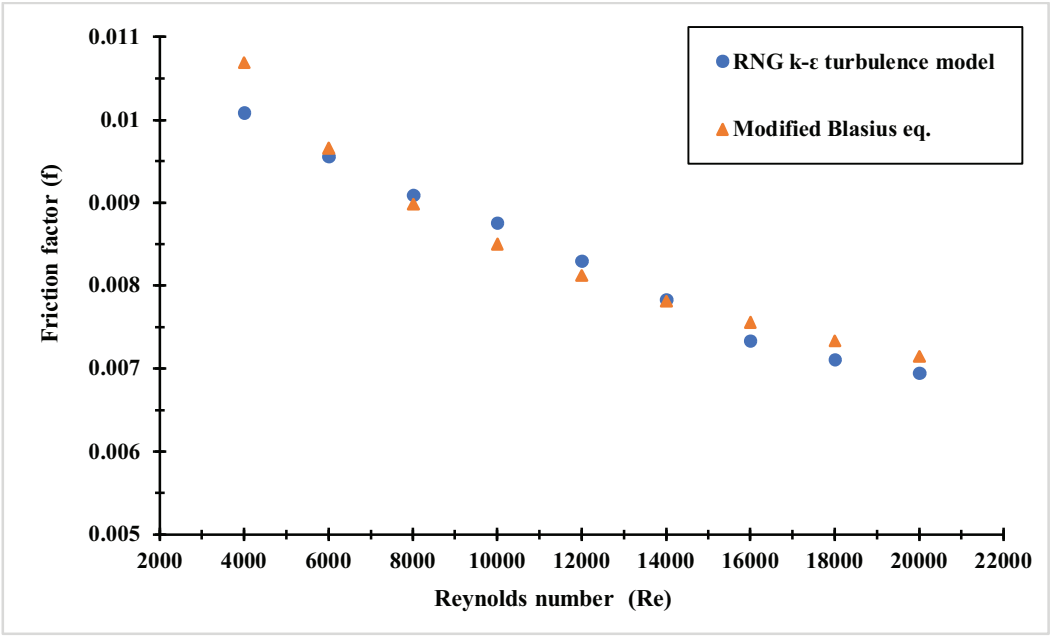


**Fig. 5.** Friction factor validation for smooth SAH duct.

**Table 3**
Boundary conditions.

| Boundary Surface | Condition |
|---|---|
| Entrance of the Duct | Ambient air with velocity varying from 1.97 to 9.87 m/s and having 300 K temperature |
| Exit of the Duct | Pressure outlet |
| Absorber Plate | Constant heat flux with a magnitude of 1000 W/m$^2$ |
| Solid and Fluid Interface | No-slip condition |
| Outside the zone | Pressure is 101325 Pascal |

were closely monitored. Convergence criteria for all the variables was fixed at $10^{-6}$. After 3500 iterations, steady-state condition was achieved and it was noticed that the solution got converged.

Solution of the governing equations require a discretization scheme [26]. A stable solution is achieved with the First order upwind discretization scheme and it also offers a better rate of residual convergence, but the results obtained may not be very much accurate and satisfactory. On the other hand, Second-order upwind scheme gives more precise solution. Thus, looking to the accuracy of the solution, Second-order upwind scheme has been employed in the current CFD exploration.

## 3. Equations employed for determination of heat transfer and friction factor

Using the outcomes of simulation, mean temperature of absorber plate, temperature of air at the exit of duct and pressure drop across the test section are determined which are further used

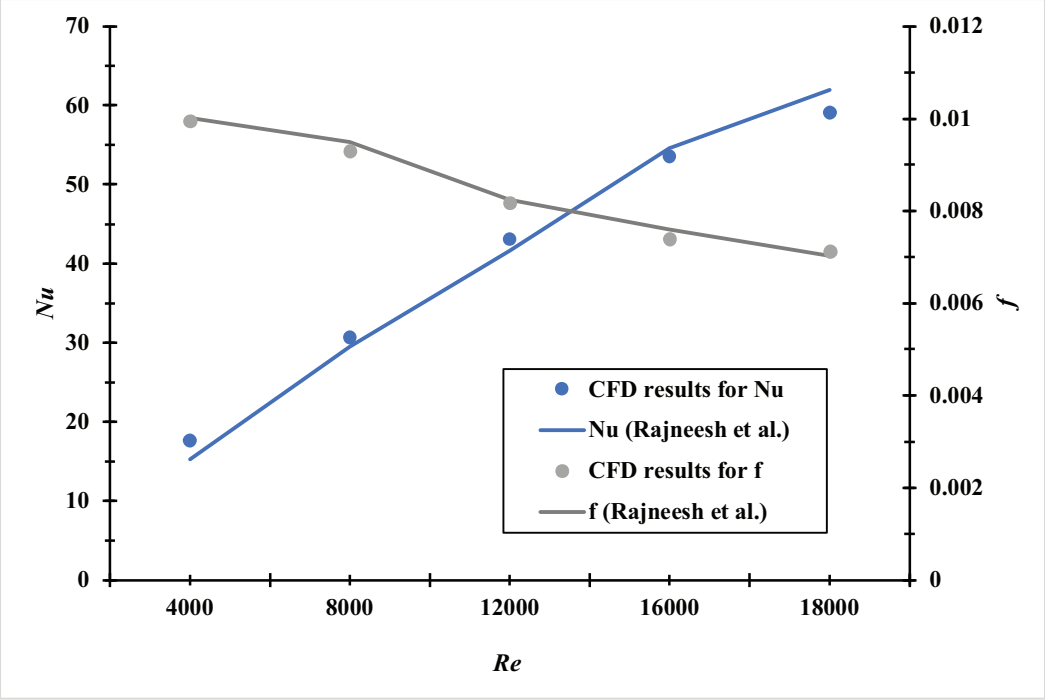


**Fig. 6.** Comparison of Nu and f values with experimental results claimed by Rajneesh et al. [1] for smooth duct.

to calculate the Nu and f. Following Equations are used in calculation:

Flow Reynolds number (Re) is yielded by,

$$Re = \frac{\rho u D_h}{\mu} \tag{6}$$

Nusselt number (Nu) is governed by following expression

$$Nu = \frac{h}{k} D_h \tag{7}$$

and the friction factor (f) is governed with the help of the formula,

$$f = \frac{1}{2\rho u^2} \times D_h \times \frac{\Delta P}{L} \tag{8}$$

## 4. Outcomes and discussion

### 4.1. Heat transfer attributes

Variation of Nusselt number (Nu) with Reynolds number (Re) for relative roughness pitch (P/e) varying from 8 to 14 at constant value of roughness height (e) = 1.2 mm and angle of attack ($\alpha$) = $60^0$ is shown in Fig. 7. From the figure, it is noted that irrespective of P/e value, Nu rises with a rise in Re. However, it is important to point out that Nu achieves its highest values at P/e = 10.

Fig. 8 depicts the effect of Nusselt number enhancement ratio (NNER) with Reynolds number at various P/e values. NNER is a key parameter, which throws light on as to how much augmentation in heat transmission is accomplished by attaching the roughness on the absorber surface compared to a smooth absorber plate. With the help of NNER, one can make a direct comparison between heat transfer characteristics of a SAH. From Fig. 8, NNER is noticed to vary in the range of 1.8-2, 1.83-2.04, 1.77-1.96 and 1.74-1.92 for different P/e values of 8, 10, 12 and 14, respectively. It is further observed that NNER attains its maximum value of 2.2 at P/e = 10 and Re = 10,000.

It is also noticed from the Fig. 8 that at all values of P/e under consideration, NNER first increases with an increase in Re, becomes maximum at Re = 10,000 and after that decreases sharply at higher Re values. The reason can be attributed to the fact that at lower Re, flow through the duct is turbulent, but still a laminar sub-layer appears over the heated absorber surface and inhibits the heat transfer, which results into relatively lower value of Nusselt number. Now, upon increasing the flow Re to 10,000, the secondary flow which moves along the ribs and escapes through the gaps mixes strongly with the primary flow and the reattachment of the flow takes place well before the consecutive ribs and minimum recirculation zone appears behind the ribs. Also, the small V-turbulence promoters help in diverting the secondary flow more and more in the inter-rib region and suppress the formation of eddies and wakes. As the Reynolds number is increased beyond 10,000, the reattachment of the main flow in the inter rib region is greatly delayed and flow reattachment usually occurs just before the next consecutive rib which drastically reduces the value of Nusselt number and heat transfer.

Fig. 9 represents the Stanton number (St) [27] variation for roughness under consideration with relative roughness pitch. It is noticed that St is highest at P/e = 10, irrespective of the flow Reynolds number. It is also noted that St declines with rise in Re and reason can be ascribed to the fact that the air being a working substance has got a Prandtl number (Pr) varying between 0.7 to 0.8 due to its poor thermal conductivity. Moreover, in all practical situations, the Pr value for air remains constant and therefore, denominator of Eq. (9) continues to increase with an increase in Re whereas, the increase in Nu is not much pronounced resulting into a decreasing trend of St with an increase in Re.

$$St = \frac{Nu}{Re * Pr} \tag{9}$$

The effect of variation of Nusselt number with Reynolds number for different $\alpha$ values is depicted in Fig. 10. It is pointed out that Nusselt number is maximum at $\alpha = 45^0$, irrespective of Re. At a value of Re, as $\alpha$ increases, Nusselt number decreases. The

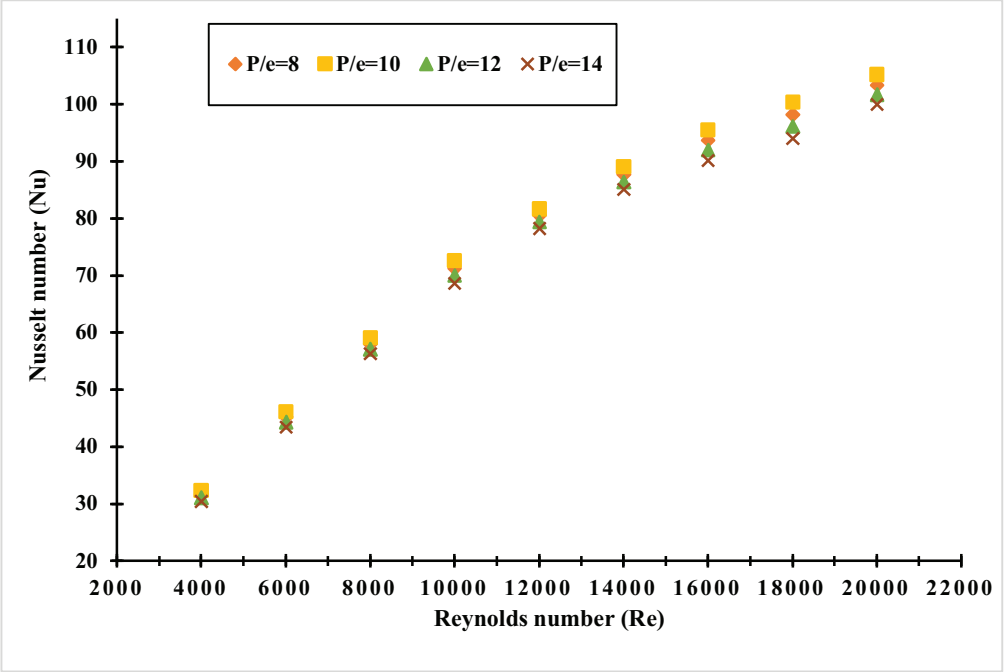


**Fig. 7.** Effect of Nu with Re for different values of P/e.

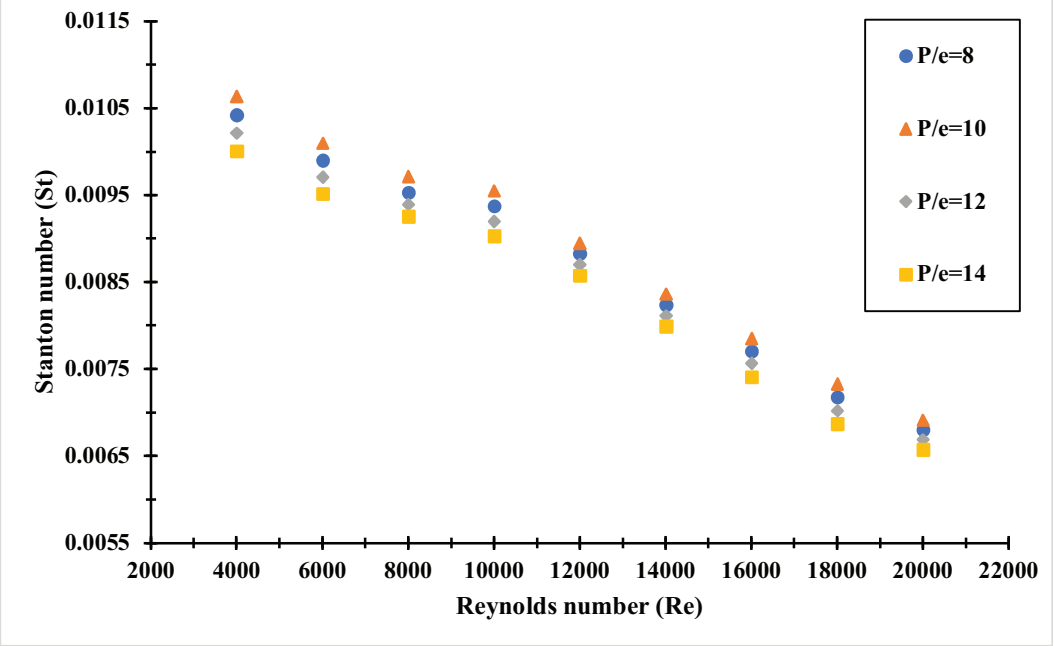


**Fig. 8.** Variation of NNER with P/e at different Re.

reason can be ascribed to the fact that as $\alpha$ increases from $45^0$ to $60^0$, the effective length of the segment of the rib reduces because the gap between the two adjacent segments is kept fixed. Now the primary flow approaches the rib and secondary flow starts travelling along the rib towards the center of the absorber plate. When $\alpha$ is $45^0$, a relatively larger length of flow takes place in the form of secondary flow from the leading edge to the trailing edge of segment. The secondary flow escapes through the gap and mixes with the primary flow and further accelerates it. This mixed flow is further diverted by the turbulence promoters resulting into greater mixing and increased turbulence levels. Upon increasing the value of $\alpha$ from $45^0$ to $60^0$, the loss in momentum of secondary flow is relatively higher and it results into a weaker secondary flow travelling along the rib and ultimately the heat transfer decreases, due to lesser and lesser turbulence levels.

Fig. 11 demonstrates NNER effect with change Re for different values of $\alpha$. As $\alpha$ is systematically rises from $45^0$ to $60^0$, NNER first increases upon increasing the Re from 4,000 to 10,000, reaches its maximum value at Re = 10,000 and thereafter, decreases sharply with an increase in Re. NNER is noticed to vary in the range of

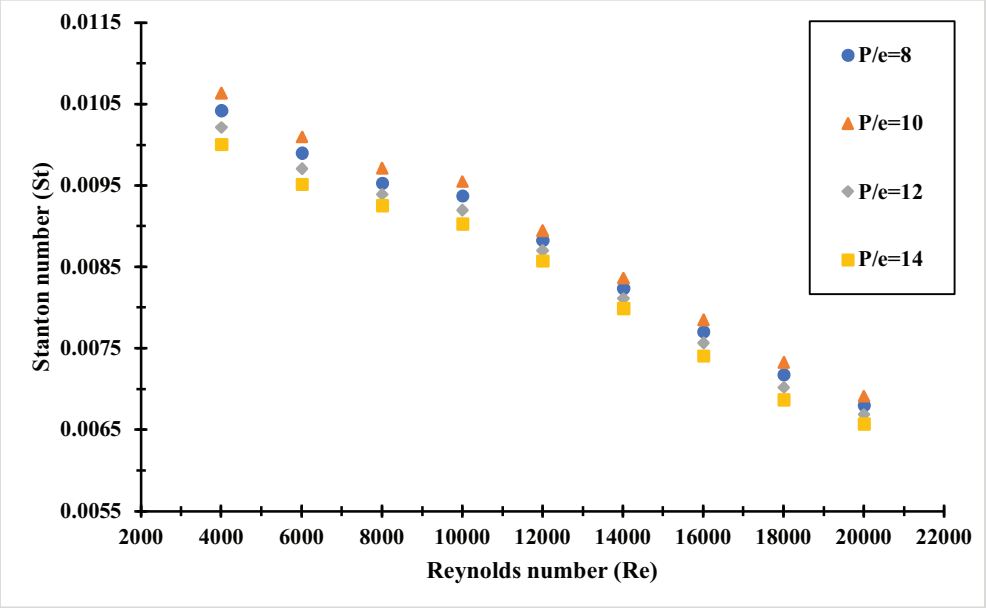


**Fig. 9.** Stanton number variation with P/e at different Re.

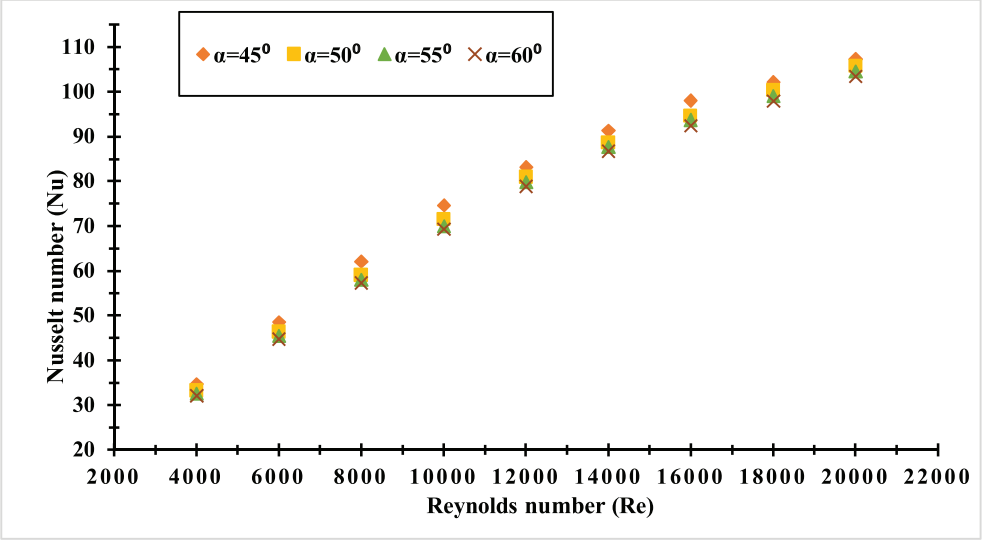


**Fig. 10.** Variation of Nu with $\alpha$ at different Re.

1.87-2.19, 1.84-2.09, 1.82-2.05 and 1.8-2.02 for different $\alpha$ values of $45^0$, $50^0$, $55^0$ and $60^0$, respectively.

Fig. 12 illustrates the effect of Stanton number for different values of $\alpha$ of roughness element. It is clearly noticed that the St attains its highest values at $\alpha = 45^0$ for all the flow Re. The reason has already been explained in the discussion part of variation of St with Re, when P/e was systematically varied.

### 4.2. Friction attributes

Effect of behaviour of friction factor with Reynolds number at different relative roughness pitch (P/e) is depicted in Fig. 13. As already pointed out that with an increase in Re, viscous sub-layer thickness reduces and therefore, f is declining with rise in Re regardless of P/e. f is found to achieve its highest value at P/e = 8 and Re = $4^*10^3$.

Fig. 14 highlights the variation of friction factor enhancement ratio (FFER) with Re when P/e is varied from 8 to 14. During this parametric study, $e/D_h = 0.04$ and $\alpha = 60^\circ$ were kept constant. Fig. 14 clearly reveals that FFER continues to rise as the Re increases from 4,000 to 16,000, attains its highest value at Re = 16,000 and decreases at further higher values of Re.

The effect of friction factor with Reynolds number for different angle of attack ($\alpha$) is represented in Fig. 15. It is noticed that as Re rises, f decreases, irrespective of $\alpha$. It is also noted that f attains its highest value of 0.014108 at $\alpha = 60^0$ and Re = 4,000. And with an increase in $\alpha$ from $45^0$ to $60^0$, f has an increasing trend.

Fig. 16 highlights the variation of FFER with Re with $\alpha$ varying from $45^0$ to $60^0$. It is noticed that FFER continues to increase as the Re increases from 4,000 to 20,000. FFER achieves its highest value at $\alpha = 60^0$ and its lowest value at $\alpha = 45^0$ for Re = 20,000.

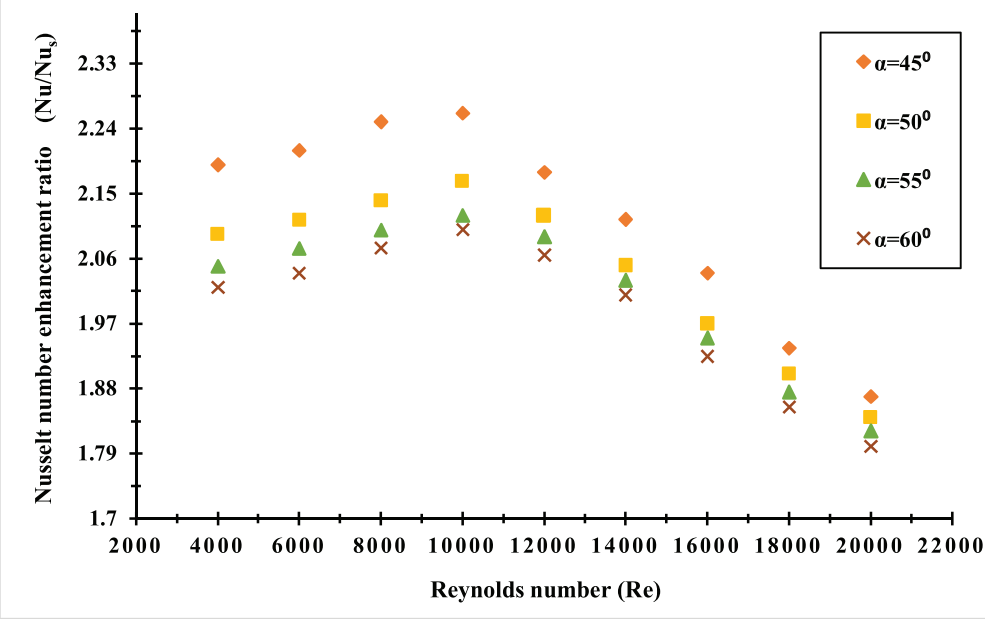


**Fig. 11.** Effect of Variation of NNER with angle of attack at different Re.

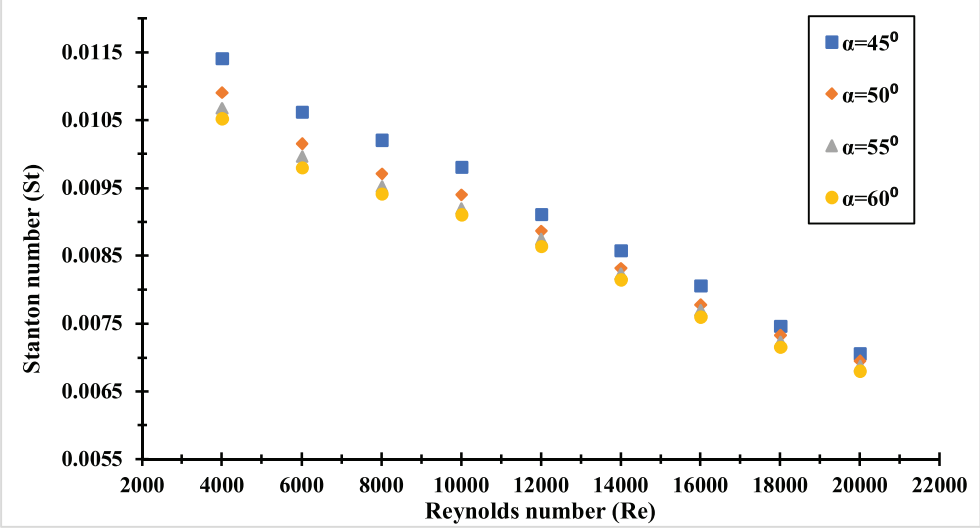


**Fig. 12.** Effect of Variation of Stanton number with angle of attack at different Re.

Figs. 17–20 show the contours of eddy viscosity plotted at the exit of test section for P/e = 8, 10, 12 and 14 at Re = 8000, 10000 and 12000, respectively. Usually, the eddy viscosity is also termed as the turbulent viscosity and is used to model the momentum transfer produced by turbulent eddies, in a similar manner as the molecular viscosity is used to model the momentum transfer produced by molecular diffusion (i.e. friction). The Boussinesq eddy viscosity assumption [28] hypotheses models the effect of turbulent eddies on the flow and this eddy viscosity is something like how viscosity is playing a role in laminar flow. The kinematic or dynamic viscosity is a fluid dependent property, whereas, the eddy viscosity is a flow dependent parameter. Viscosity causes shear stress in response to shearing of the flow. Eddies cause a similar effect, but they do it by physically moving faster fluid into slower regions and moving slower fluid into faster regions. Lots of little eddies make the fluid behave as though it had more viscosity. The internal fluid friction caused by eddies is taking place on a larger scale, is analogous to the molecular viscosity action in laminar flow. It is noticed that at P/e = 12 and Re = 10000, minimum area is covered with larger eddy viscosity value, which means a much lesser internal fluid friction.

Figs. 21–24 portray the contours of eddy viscosity for $\alpha = 45°$, 50°, 55° and 60° at Re = 8000, 10000 and 12000, respectively. It is noted that at $\alpha = 45°$ and Re = 12000, eddy viscosity with higher value has a minimum region, reflecting relatively lesser internal fluid friction.

A term called as Helicity is being discussed here to authenticate the results and findings of simulation work. The motion of each fluid element can be described as the sum of a translation, rotation, and deformation and the degree of local rotation in the fluid is measured in terms of vorticity. The helicity is the dot product of the vorticity and velocity vectors and it provides insight

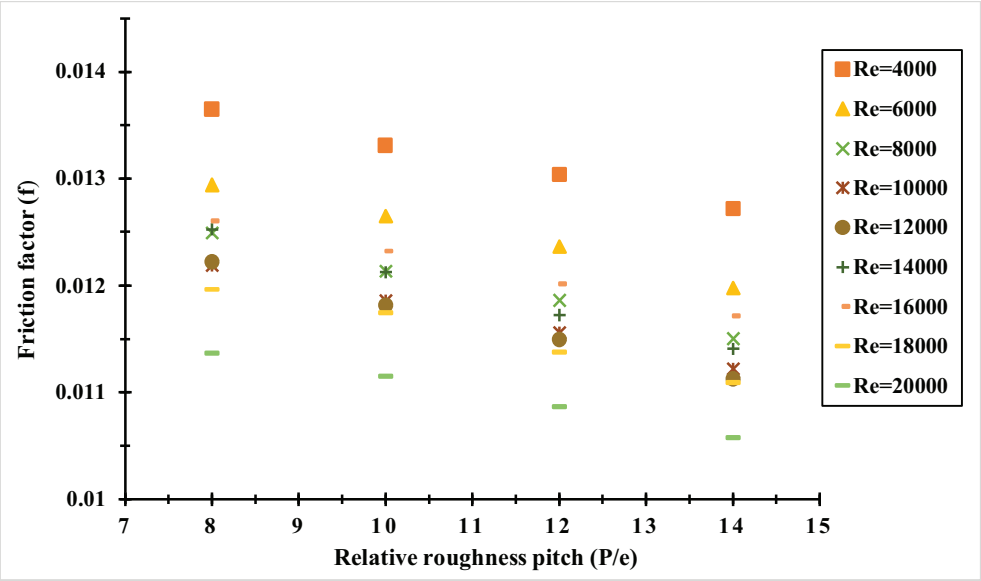


**Fig. 13.** Variation of f with P/e at different Re.

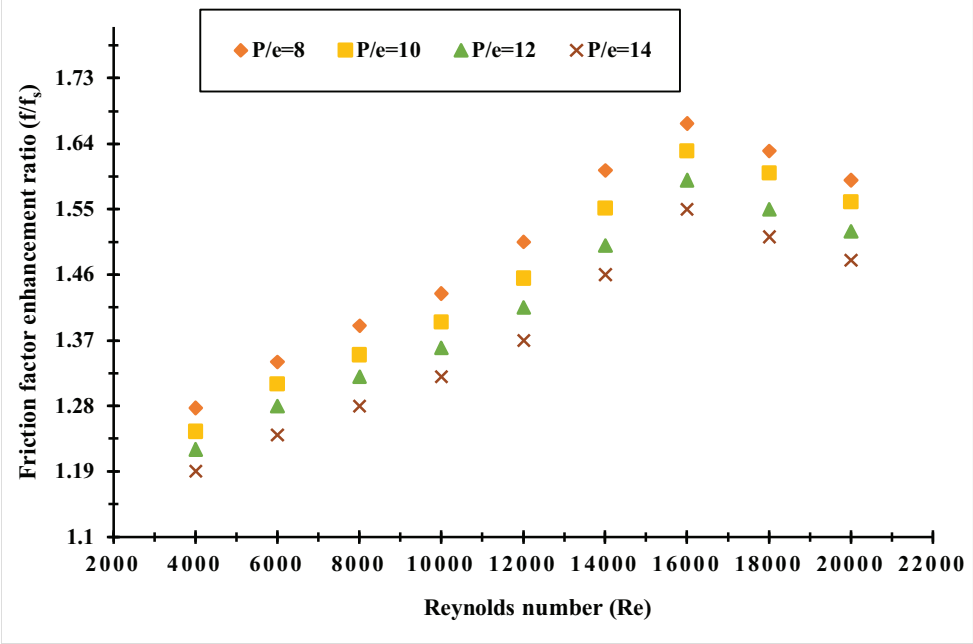


**Fig. 14.** Effect of FFER with relative roughness pitch at different Re.

into how the vorticity vector and the velocity vector are aligned. Helicity plays an important role in characterizing complex three-dimensional flows including mixing, loss of stability, transition to turbulence and vortex breakdown.

Figs. 25–28 shows the contours of Helicity density [29] plotted at the exit of test section for different P/e values and at different Re. In the contours, the region highlighted with red and yellow color demonstrates the primary high-pressure vortices and the region marked with blue color shows the alteration in helicity density due to break-down of primary vortex into induced vortex. It is observed that as flow Re increases, the strength of primary as well as induced vortex also increases, which is reflected by much broader and denser red and blue zones. It is further noticed that at P/e = 10 and Re = 12000, highest helicity density is attained.

Similarly, upon varying the angle of attack from 45° to 60° at different Re, contours of Helicity plots are depicted in Figs. 29–32. It is noticed that at $\alpha = 45°$, maximum Helicity density is observed irrespective of flow Re.

### 4.3. Thermo-hydraulic performance parameter

Thermo-hydraulic performance parameter (THPP) [30] is a vital term, which conveys the thermal and frictional response of a roughened SAH in a more convincing way. It correlates the NNER

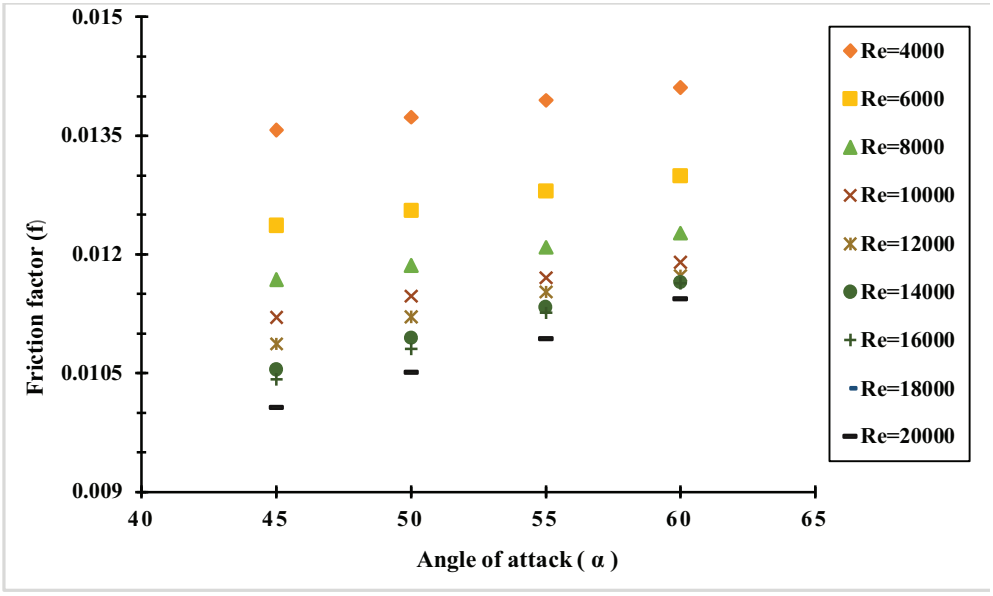


**Fig. 15.** Effect of f with $\alpha$ at different Re.

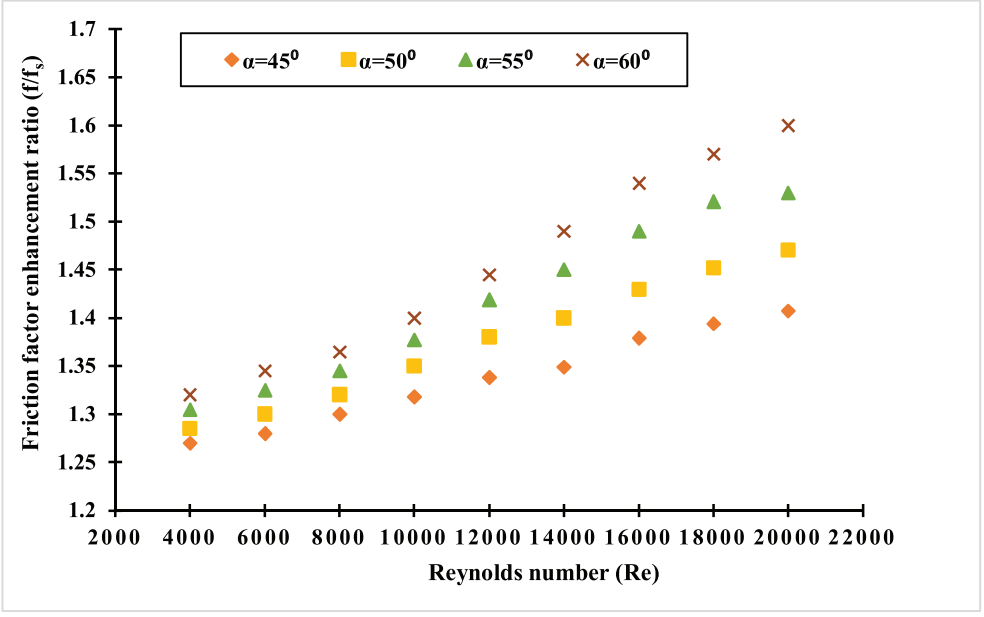


**Fig. 16.** Effect of FFER with $\alpha$ at different Re.

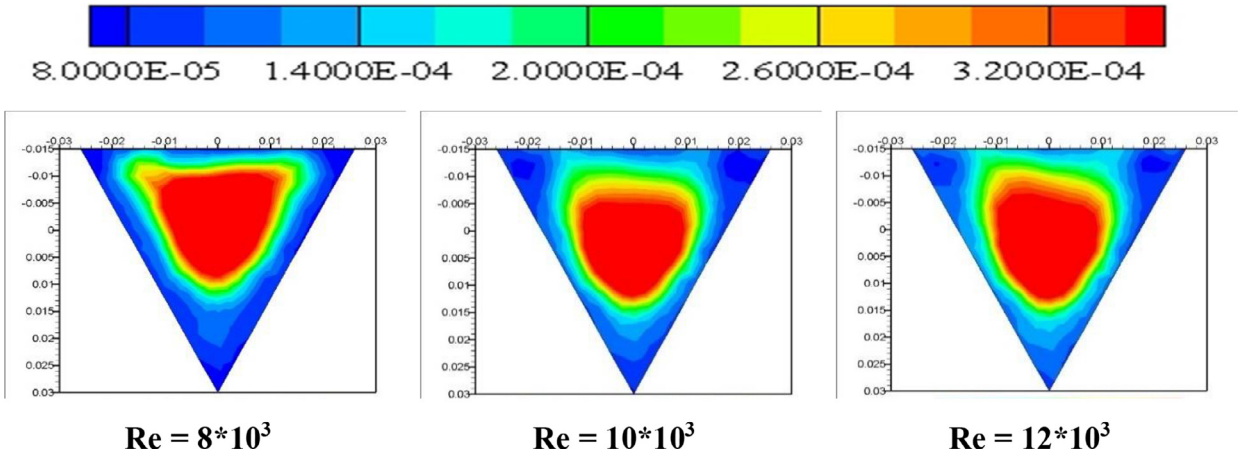


**Fig. 17.** Contours of Eddy Viscosity for different Re at P/e = 8.

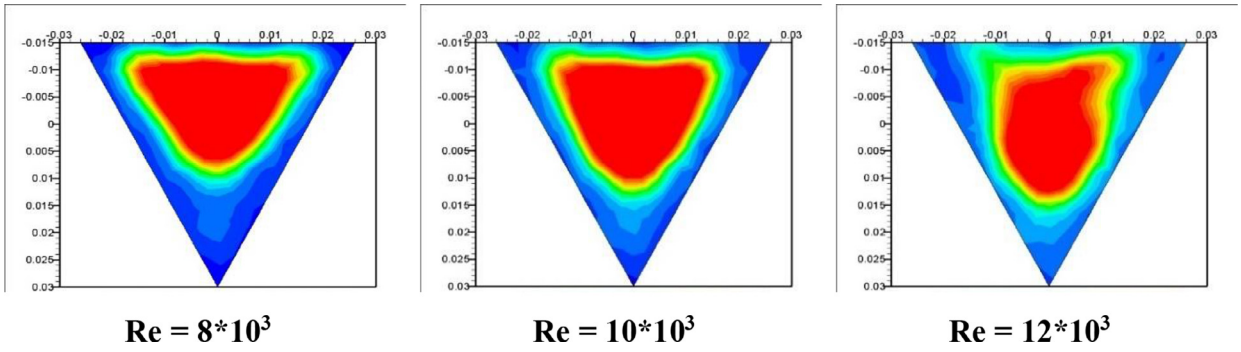


**Fig. 18.** Contours of Eddy Viscosity for different Re at P/e = 10.

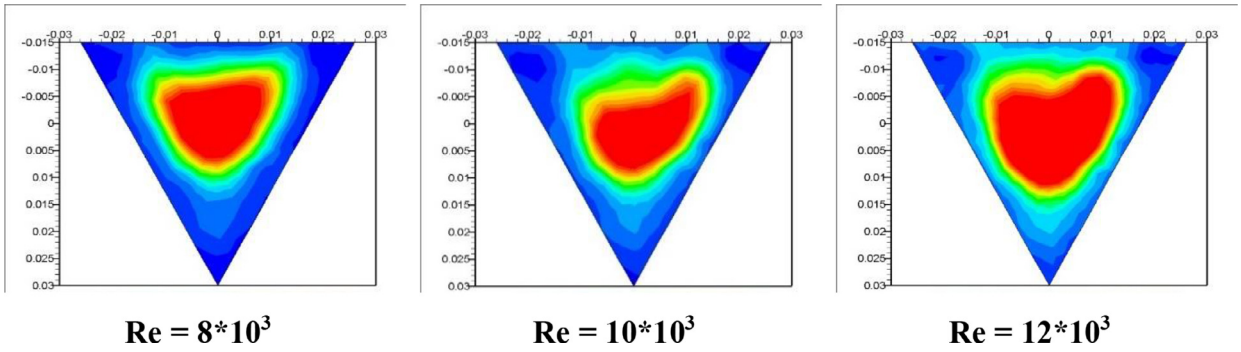


**Fig. 19.** Contours of Eddy Viscosity for different Re at P/e = 12.

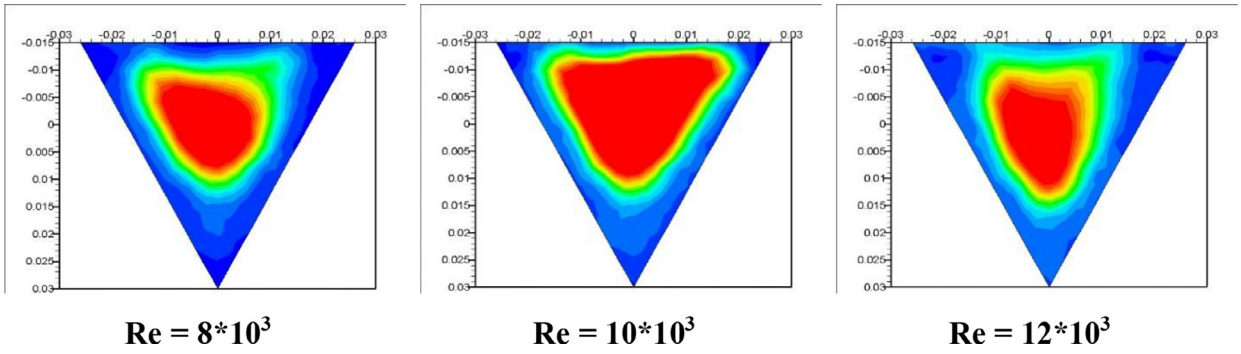


**Fig. 20.** Contours of Eddy Viscosity for different Re at P/e = 14.

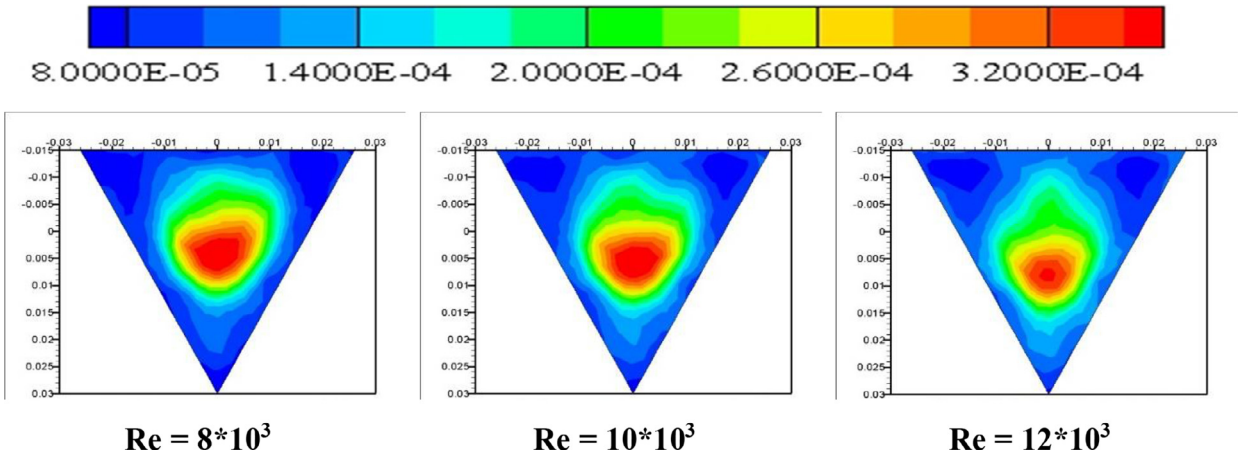


**Fig. 21.** Contours of Eddy Viscosity for different Re at $\alpha = 45°$.

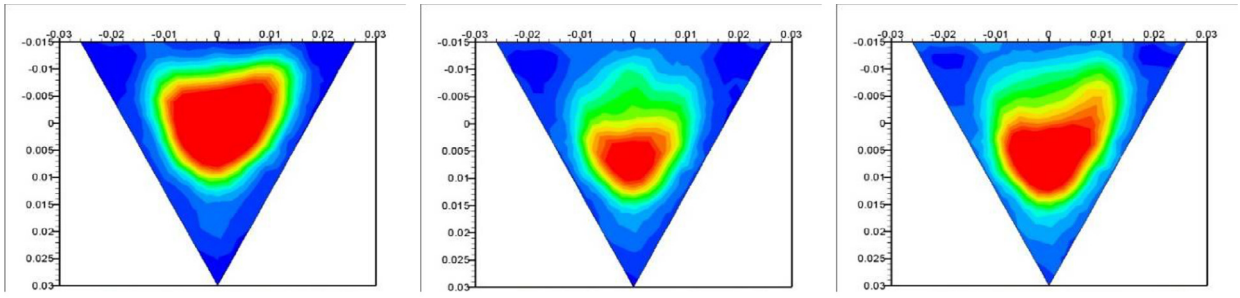


**Fig. 22.** Contours of Eddy Viscosity for different Re at $\alpha = 50°$.

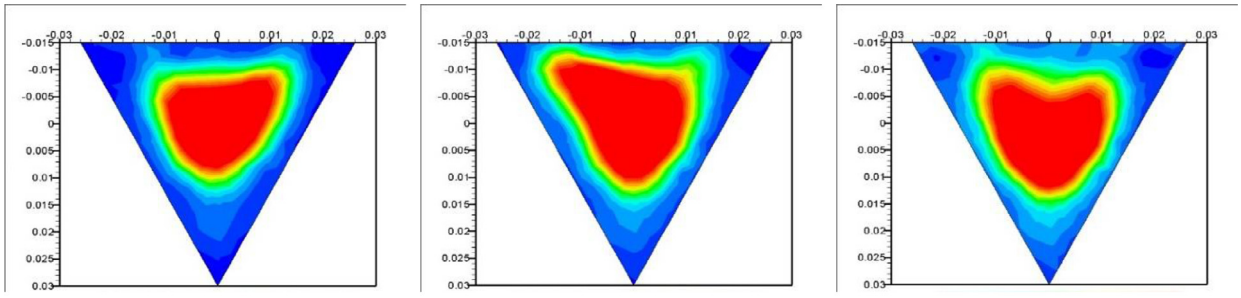


**Fig. 23.** Contours of Eddy Viscosity for different Re at $\alpha = 55°$.

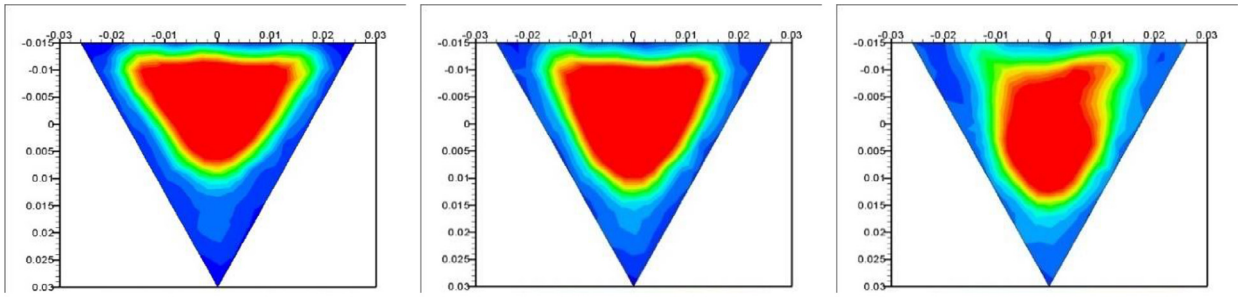


**Fig. 24.** Contours of Eddy Viscosity for different Re at $\alpha = 60°$.

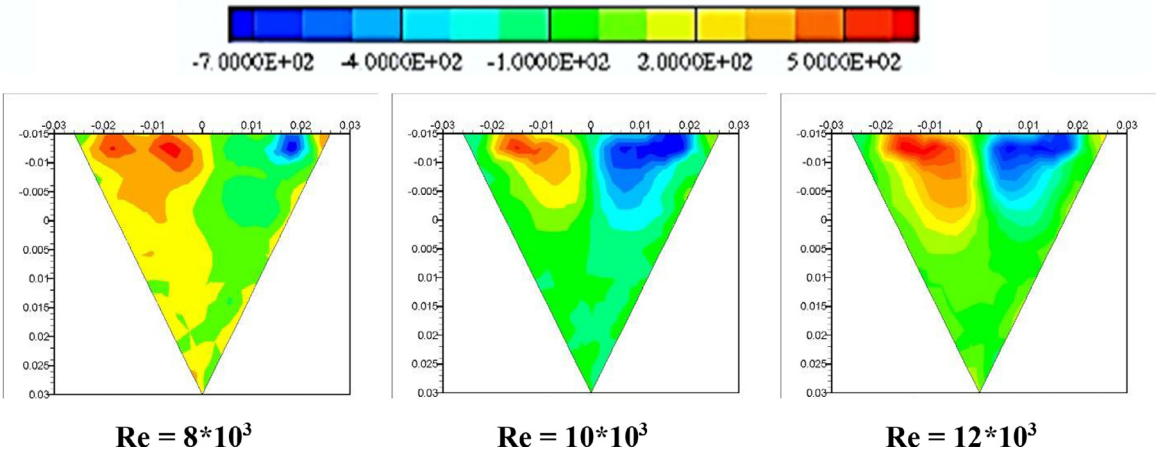


**Fig. 25.** Contours of Helicity for different Re at P/e = 8.

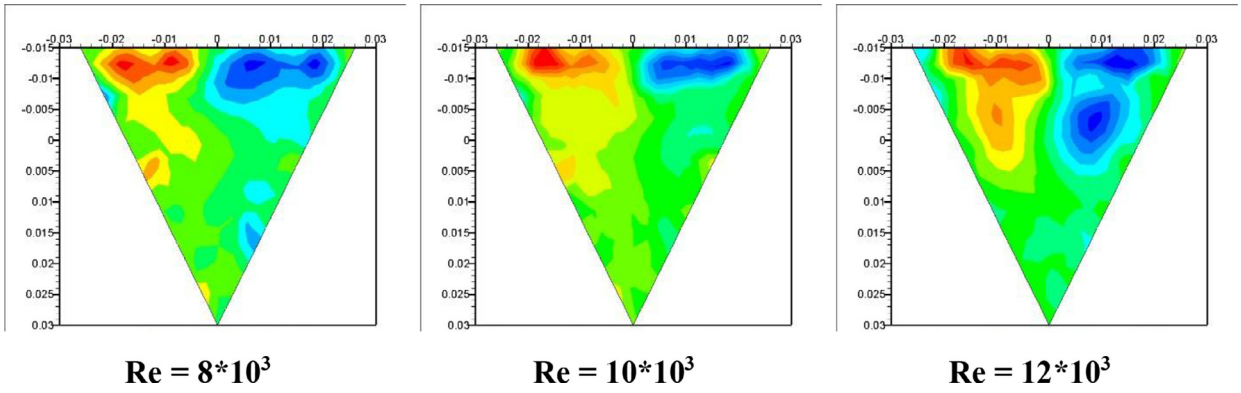


**Fig. 26.** Contours of Helicity for different Re at P/e = 10.

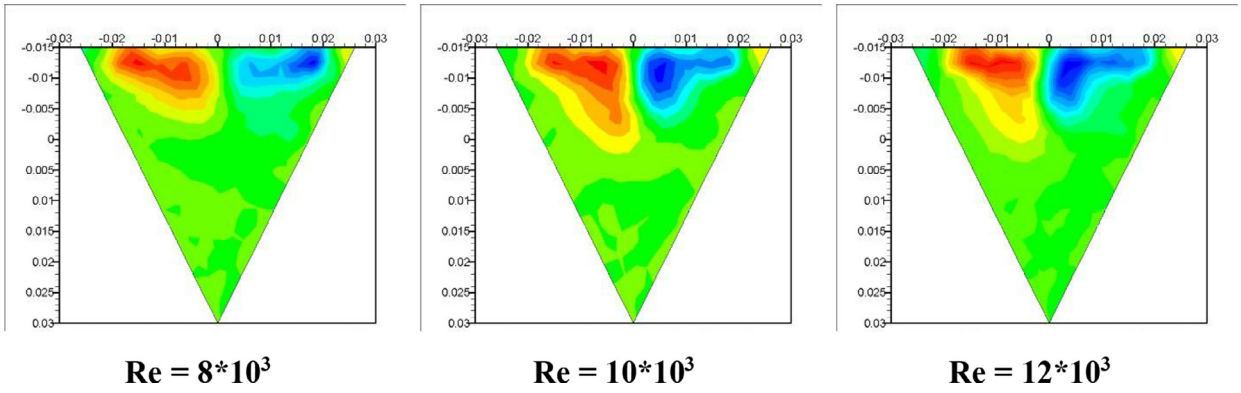


**Fig. 27.** Contours of Helicity for different Re at P/e = 12.

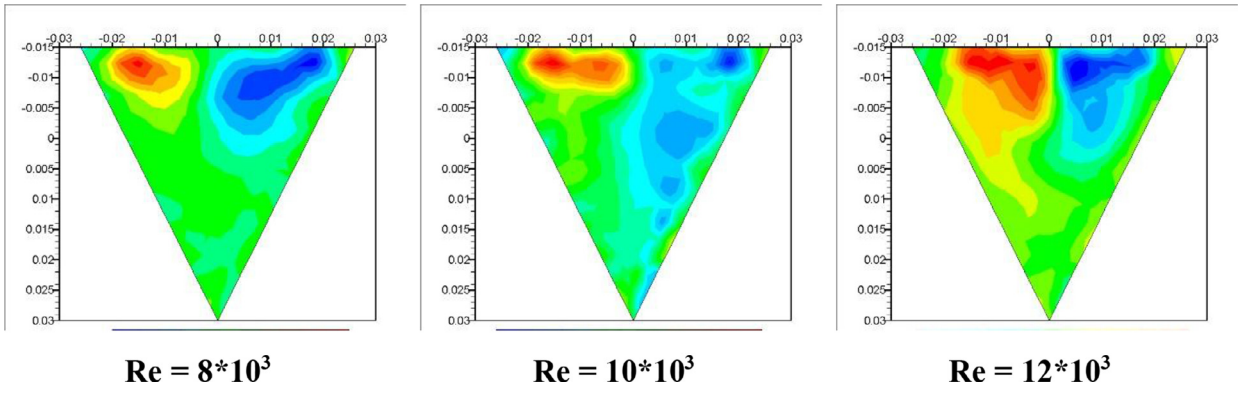


**Fig. 28.** Contours of Helicity for different Re at P/e = 14.

$(Nu/Nu_s)$ with FFER $(f/f_s)$ [31]. With the aim of boosting the heat transmission from the absorber surface, the usefulness of roughness is said to be justified if THPP attains a value greater than 1, irrespective of flow Re. Needless to mention that the improvement in heat transfer by using the artificial roughness also invites a considerable increase in friction factor. Thus, the attachment of roughness is feasible if the heat transfer improves with minimum pressure loss. THPP is given as;

$$\mathrm{THPP} = \frac{\left(\frac{\mathrm{Nu}}{\mathrm{Nu_s}}\right)}{\left(\frac{\mathrm{f}}{\mathrm{f_s}}\right)^{0.33}} \tag{10}$$

Figs. 33 and 34 demonstrates the THPP variation with Re for P/e and $\alpha$ values, respectively. It is concluded that the mounting of V- down rib with multiple gaps and turbulence promoters on the underneath of the absorber surface, gives better heat transfer from absorber surface to air in contrast to smooth absorber plate. It is further noticed that THPP is found to be maximum having a value of 2.064 at P/e = 10 and $\alpha = 45^0$.

### *4.4. Evaluation of current roughness with former researchers' roughness*

In order to prove the worth and usefulness, a comparison of NNER, FFER and THPP obtained for current investigation has been contrasted with former researchers' roughness, is portrayed in Table 4. It is observed that with the proposed roughness, maximum THPP of 2.064 is obtained, which is greater than the THPP values asserted for roughness patterns examined by researchers' including [32,33] and [5]. Thus, the SAH with V-down rib with multiple gaps and turbulence promoters as artificial roughness

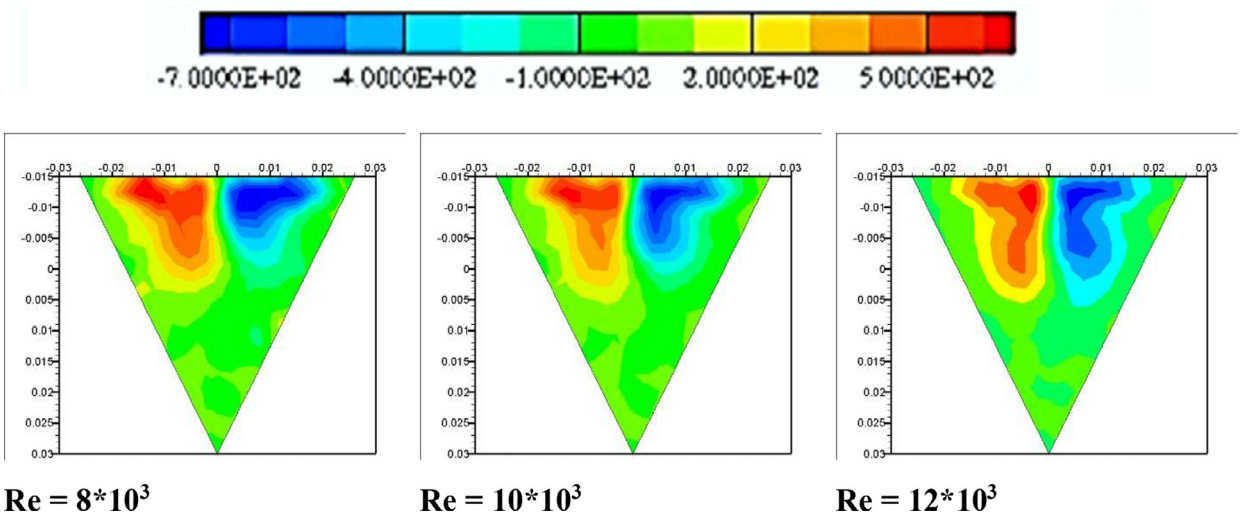


**Fig. 29.** Contours of Helicity for different Re at $\alpha = 45°$.

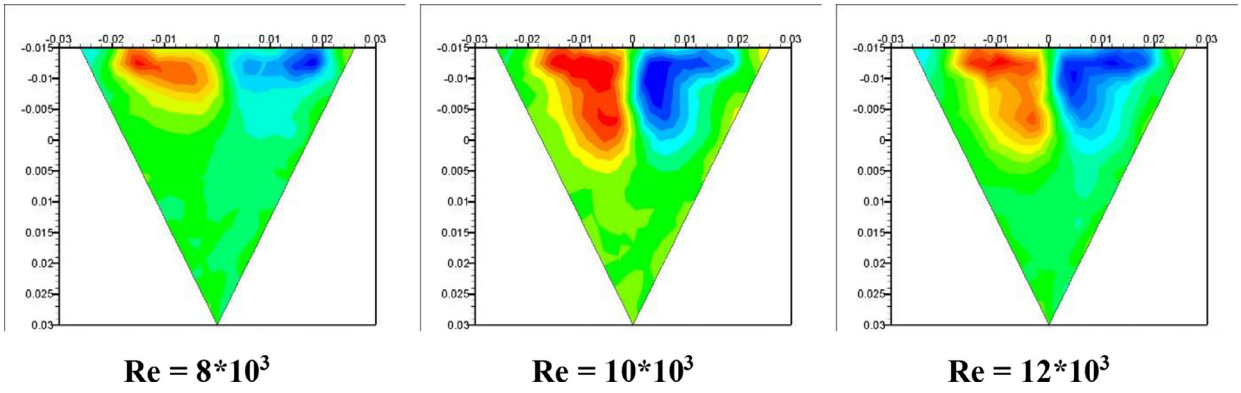


**Fig. 30.** Contours of Helicity for different Re at $\alpha = 50°$.

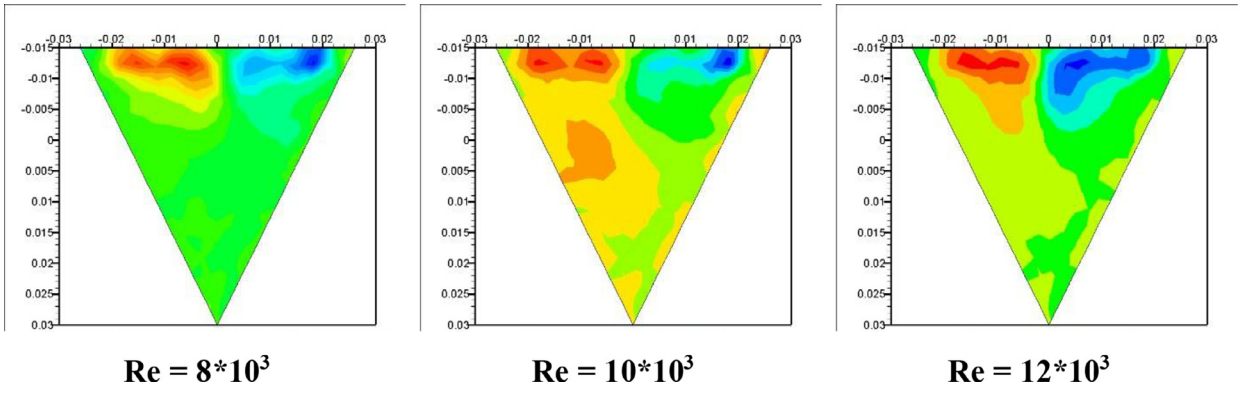


**Fig. 31.** Contours of Helicity for different Re at $\alpha = 55°$.

**Table 4**
NNER, FFER and THPP for proposed roughness in contrast to former researchers' roughness.

| S. No. | Authors | Artificial roughness pattern | NNER | FFER | THPP |
|---|---|---|---|---|---|
| 1. | Kumar et al. [32] | Rectangular transverse ribs | 2.3 | 4.5 | 1.89 |
| 2. | Kumar et al. [33] | Semi-circular transverse rib | 2.2 | 2.5 | 1.7 |
| 3. | Jain et al. [5] | Broken inclined ribs having rectangular cross-section | 2.16 | 2.4 | 1.98 |
| 4. | Patel and Lanjewar [8] | V-rib roughness | 2.26 | 3.40 | 1.59 |
| 5. | Present study | V-down rib with multiple gaps and turbulence promoters | 2.26 | 1.6 | 2.064 |

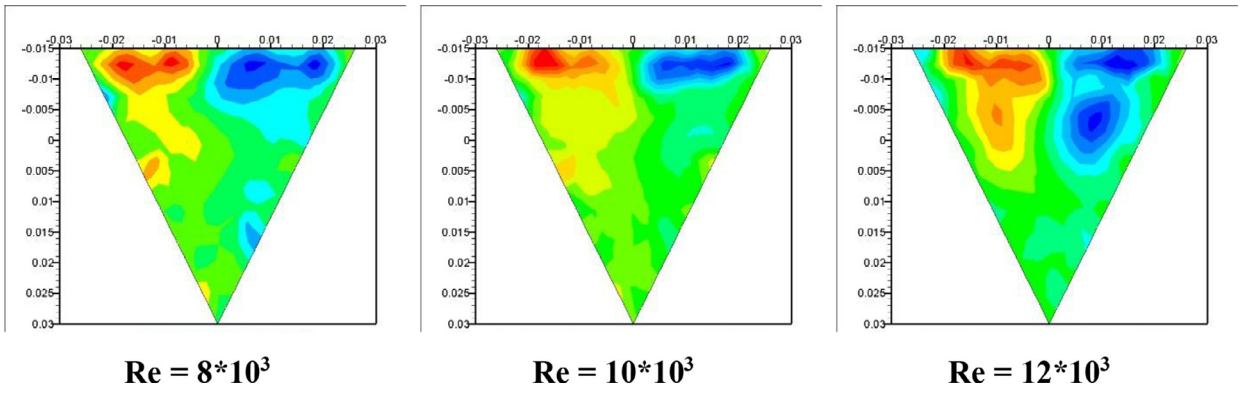


**Fig. 32.** Contours of Helicity for different Re at $\alpha = 60°$.

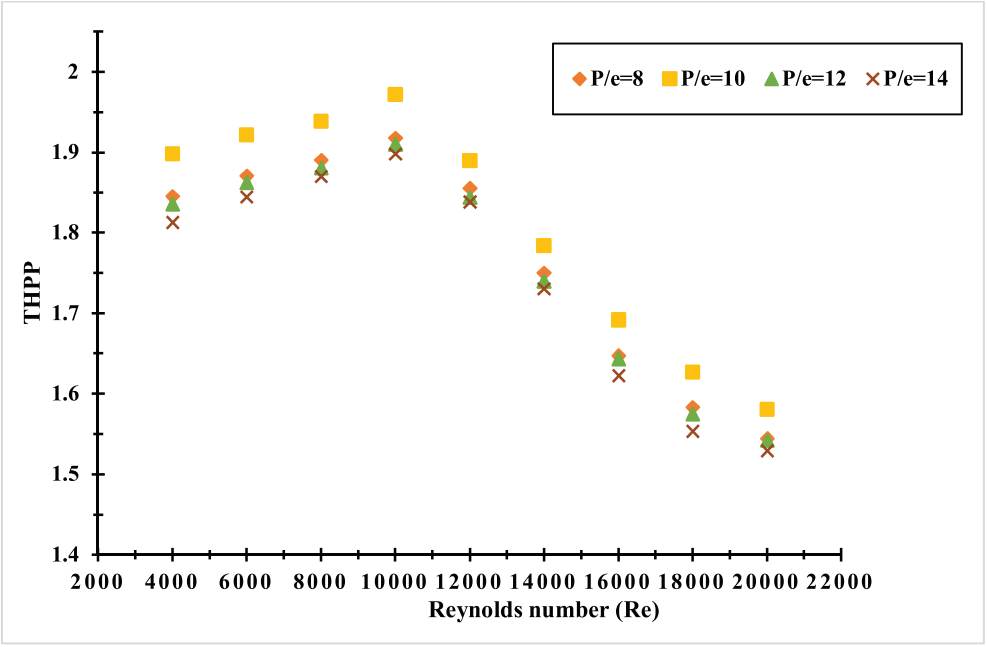


**Fig. 33.** Variation of THPP with Re for various P/e values.

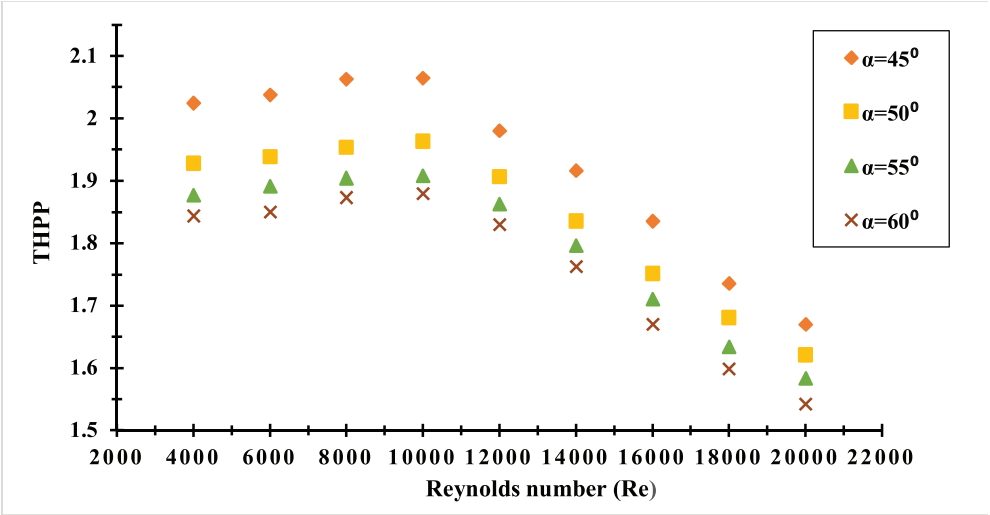


**Fig. 34.** Variation of THPP with Re for various $\alpha$ values.

turns out to be much advantageous than other roughness geometries examined recently.

## 5. Conclusions

A numerical exploration has been conducted to analyze the thermo-hydraulic performance of a triangular SAH duct whose absorber plate is artificially roughened with V-down rib with multiple gaps and turbulence promoters. The geometric domain is developed using SOLIDWORKS (18.0) and same was imported in ANSYS FLUENT (19.0) for further analysis. During the study, relative roughness pitch (P/e) and angle of attack ($\alpha$) were systematically varied from 8 to 14 (4 values) and $45^0$ to $60^0$ (4 values), respectively. Reynolds number (Re) was also varied from 4,000 to 20,000. However, relative roughness height ($e/D_h$) and hydraulic diameter ($D_h$) were kept constant. Total 63 simulation runs were carried out on 7 different geometries. Study concludes as follows;

1 Using V-down rib with multiple gaps and turbulence promoters as artificial roughness leads to an enrichment in heat transfer and fluid flow behavior both, because of enhanced level of interaction among the fluid particles.
2 Upon varying relative roughness pitch (P/e) from 8 to 14 and angle of attack ($\alpha$) from $45^0$ to $60^0$, maximum heat transfer rate is attained at P/e = 10 and $\alpha = 45^0$, respectively, irrespective of Reynolds number.
3 At P/e = 10, $\alpha = 45^0$ and Re = 10,000, Nusselt number enhancement ratio attains its maximum value of 2.26, as the flow reattaches before the consecutive ribs and this leads to proper mixing of the secondary flow with the primary flow.
4 As compared to smooth SAH duct, friction factor for SAH duct roughened with proposed roughness is found to be maximum at P/e = 10, $\alpha = 60^0$ and Re = 20,000.
5 On varying friction factor with P/e for different Re demonstrates that the f declines irrespective of P/e and Re and its highest value is at P/e = 8 and Re = 4,000.
6 On varying P/e from 8 to 14 and $\alpha$ from 45° to 60° for Re = 8000, 10000 and 12000, the contours of eddy viscosity illustrate that for P/e = 12 at Re = 10000 and for $\alpha = 45°$ at Re = 12000, the region covered with larger values of eddy viscosity is minimum.
7 The highest Helicity density is achieved at P/e = 10 and Re = 12000. It is also noted that as the angle of attack varies from 45° to 60° at different Re, maximum Helicity density is observed at $\alpha = 45°$, irrespective of flow Re.
8 THPP increases upon increasing the Re from 4000 to 10,000, attains its maximum value and thereafter, decreases at higher Re, as the flow becomes highly turbulent.

## Author statement

All the authors have contributed equally in preparing this manuscript.

## Declaration of Competing Interest

The authors declare that they have no known competing financial interests or personal relationships that could have appeared to influence the work reported in this paper.

## Acknowledgement

The authors are indebted to AICTE, New Delhi, India for providing financial assistance under Collaborative Research Scheme (CRS) Vide grant no. CRS/1-5766820846 for conducting the study.

## References

[1] R. Kumar, A.Kumar Varun, Experimental and computational fluid dynamics study on fluid flow and heat transfer in triangular passage solar air heater of different configurations, J. Sol. Energy Eng. 139 (2017) 041013, doi:10.1115/1.4036775.
[2] R. Kumar, V. Goel, P. Singh, A. Saxena, A.S. Kashyap, A. Rai, Performance evaluation and optimization of solar assisted air heater with discrete multiple arc shaped ribs, J. Energy Storage 26 (2019) 100978, doi:10.1016/j.est.2019.100978.
[3] S.K. Jain, R. Misra, A. Kumar, G. Das Agrawal, Thermal performance investigation of a solar air heater having discrete V-shaped perforated baffles, Int. J. Ambient Energy 0 (2019) 1–9, doi:10.1080/01430750.2019.1636874.
[4] R. Kumar, V. Goel, A. Kumar, S. Khurana, P. Singh, S.B. Bopche, Numerical investigation of heat transfer and friction factor in ribbed triangular duct solar air heater using computational fluid dynamics (CFD), J. Mech. Sci. Technol. 32 (2018) 399–404, doi:10.1007/s12206-017-1240-8.
[5] S.K. Jain, G. Das Agrawal, R. Misra, P. Verma, S. Rathore, D.K. Jamuwa, Performance investigation of a triangular solar air heater duct having broken inclined roughness using computational fluid dynamics, J. Sol. Energy Eng. Trans. ASME 141 (2019) 1–11, doi:10.1115/1.4043751.
[6] S.K. Jain, G. Das Agrawal, R. Misra, Heat transfer augmentation using multiple gaps in arc-shaped ribs roughened solar air heater: an experimental study, Energy Sources Part A Recover. Util. Environ. Eff. 0 (2019) 1–12, doi:10.1080/15567036.2019.1607945.
[7] R. Kumar, A. Kumar, V. Goel, Simulation of flow and heat transfer in triangular cross-sectional solar-assisted air heater, J. Sol. Energy Eng. Trans. ASME 141 (2019), doi:10.1115/1.4041098.
[8] S. Singh Patel, A. Lanjewar, Experimental and numerical investigation of solar air heater with novel V-rib geometry, J. Energy Storage 21 (2019) 750–764, doi:10.1016/j.est.2019.01.016.
[9] I. Singh, S. Vardhan, S. Singh, A. Singh, Experimental and CFD analysis of solar air heater duct roughened with multiple broken transverse ribs: a comparative study, Sol. Energy 188 (2019) 519–532, doi:10.1016/j.solener.2019.06.022.
[10] I. Singh, S. Singh, CFD analysis of solar air heater duct having square wave profiled transverse ribs as roughness elements, Sol. Energy 162 (2018) 442–453, doi:10.1016/j.solener.2018.01.019.
[11] B.S. Qader, E.E. Supeni, M.K.A. Ariffin, A.R.A. Talib, Numerical investigation of flow through inclined fins under the absorber plate of solar air heater, Renew. Energy 141 (2019) 468–481, doi:10.1016/j.renene.2019.04.024.
[12] P.K. Jain, A. Lanjewar, Overview of V-RIB geometries in solar air heater and performance evaluation of a new V-RIB geometry, Renew. Energy 133 (2019) 77–90, doi:10.1016/j.renene.2018.10.001.
[13] A. Perwez, R. Kumar, Thermal performance investigation of the flat and spherical dimple absorber plate solar air heaters, Sol. Energy 193 (2019) 309–323, doi:10.1016/j.solener.2019.09.066.
[14] V. Kumar, Nusselt number and friction factor correlations of three sides concave dimple roughened solar air heater, Renew. Energy 135 (2019) 355–377, doi:10.1016/j.renene.2018.12.002.
[15] P.T. Saravanakumar, D. Somasundaram, M.M. Matheswaran, Thermal and thermo-hydraulic analysis of arc shaped rib roughened solar air heater integrated with fins and baffles, Sol. Energy 180 (2019) 360–371, doi:10.1016/j.solener.2019.01.036.
[16] P. Promvonge, S. Skullong, Heat transfer augmentation in solar receiver heat exchanger with hole-punched wings, Appl. Therm. Eng. 155 (2019) 59–69, doi:10.1016/j.applthermaleng.2019.03.132.
[17] J. Ambade, A. Lanjewar, Experimental investigation of solar air heater with new symmetrical GAP ARC GEOMETRY and staggered element, Int. J. Therm. Sci. 146 (2019) 106093, doi:10.1016/j.ijthermalsci.2019.106093.
[18] M.T. Baissi, A. Brima, K. Aoues, R. Khanniche, N. Moummi, Thermal behavior in a solar air heater channel roughened with delta-shaped vortex generators, Appl. Therm. Eng. 165 (2020) 113563, doi:10.1016/j.applthermaleng.2019.03.134.
[19] A. Kumar, A. Layek, Nusselt number and fluid flow analysis of solar air heater having transverse circular rib roughness on absorber plate using LCT and computational technique, Therm. Sci. Eng. Prog. 14 (2019) 100398, doi:10.1016/j.tsep.2019.100398.
[20] S. Debnath, B. Das, P. Randive, Influences of pentagonal ribs on the performance of rectangular solar air collector, Energy Procedia 158 (2019) 1168–1173, doi:10.1016/j.egypro.2019.01.300.
[21] T. Cebeci, P. Bradshaw, Physical and Computational Aspects of Covective Heat Transfer, Springer-Verlag, Berlin Heidelberg GmbH, 1984, doi:10.1007/978-3-662-02411-9.
[22] J.E. Hill, Method of Testing Performance for Rating Solar Collectors Based on Thermal, (1974).
[23] F. Menasria, M. Zedairia, A. Moummi, Numerical study of thermohydraulic performance of solar air heater duct equipped with novel continuous rectangular baffles with high aspect ratio, Energy 133 (2017) 593–608, doi:10.1016/j.energy.2017.05.002.
[24] Ansys Inc., in: Ansys Fluent 15.0 - Theory Guide, 15317, ANSYS Inc., USA, 2010, pp. 0–746.
[25] V.B. Gawande, A.S. Dhoble, D.B. Zodpe, S. Chamoli, Experimental and CFD investigation of convection heat transfer in solar air heater with reverse L-shaped ribs, Sol. Energy 131 (2016) 275–295, doi:10.1016/j.solener.2016.02.040.
[26] D.S. Thakur, M.K. Khan, M. Pathak, Solar air heater with hyperbolic ribs: 3D simulation with experimental validation, Renew. Energy 113 (2017) 357–368, doi:10.1016/j.renene.2017.05.096.

[27] R. Karwa, G. Chitoshiya, Performance study of solar air heater having v-down discrete ribs onabsorber plate, Energy 55 (2013) 939–955, doi:10.1016/j.energy.2013.03.068.
[28] F.G. Schmitt, About Boussinesq's turbulent viscosity hypothesis: historical remarks and a direct evaluation of its validity, Comptes Rendus - Mec. 335 (2007) 617–627, doi:10.1016/j.crme.2007.08.004.
[29] P.J. Bezbaruah, R.S. Das, B.K. Sarkar, Thermo-hydraulic performance augmentation of solar air duct using modified forms of conical vortex generators, Heat Mass Transf. Und Stoffuebertragung 55 (2019) 1387–1403, doi:10.1007/s00231-018-2521-1.
[30] R.L. Webb, E.R.G. Eckert, Application of rough surfaces to heat exchanger design, Int. J. Heat Mass Transf. 15 (1972) 1647–1658, doi:10.1016/0017-9310(72)90095-6.
[31] R. Karwa, B.K. Maheshwari, N. Karwa, Experimental study of heat transfer enhancement in an asymmetrically heated rectangular duct with perforated baffles, Int. Commun. Heat Mass Transf. 32 (2005) 275–284, doi:10.1016/j.icheatmasstransfer.2004.10.002.
[32] R. Kumar, A. Kumar, V. Goel, A parametric analysis of rectangular rib roughened triangular duct solar air heater using computational fluid dynamics, Sol. Energy 157 (2017) 1095–1107, doi:10.1016/j.solener.2017.08.071.
[33] R. Kumar, A. Kumar, Varun, Computational fluid dynamics based study for analyzing heat transfer and friction factor in semi-circular rib-roughened equilateral triangular duct, Int. J. Numer. Methods Heat Fluid Flow 27 (2017) 941–957, doi:10.1108/HFF-10-2015-0438.